Evidence from Fe- and Al-rich metapelites for thrust loading in the Transangarian region of the Yenisey Ridge, eastern Siberia

I. I. LIKHANOV[1], O. P. POLYANSKY[1], V. V. REVERDATTO[1] AND I. MEMMI[2]

[1]*Institute of Mineralogy and Petrography, Siberian Branch, Russian Academy of Sciences, Pr. Acad. Koptyuga 3, Novosibirsk 630090, Russia (likh@uiggm.nsc.ru)*
[2]*University of Siena, Via Laterina 8, 53100 Siena, Italy*

ABSTRACT   In the Transangarian region of the Yenisey Ridge in eastern Siberia (Russia), Fe- and Al-rich metapelitic schists of the Korda plate show field and petrological evidence of two superimposed metamorphic events. An early middle Proterozoic event with age of *c.*1100 Ma produced low-pressure, andalusite-bearing assemblages at *c.* 3.5–4 kbar and 540–560 °C. During a subsequent late Proterozoic event at *c.* 850 Ma, a medium-pressure, regional metamorphic overprint produced kyanite-bearing mineral assemblages that replaced minerals formed in the low-pressure event. Based on the results of geothermobarometry and *P–T* path calculations it can be shown that pressure increased from 4.5 to 6.7 kbar at a relatively constant temperature of 540–600 °C towards a major suture zone called the Panimba thrust. In order to produce such nearly isothermal loading of 1–7 °C km $^{-1}$, we propose a model for the tectono-metamorphic evolution of the study area based on crustal thickening caused by south-westward thrusting of the 5–7 km-thick upper-plate metacarbonates over lower-plate metapelites with velocity of *c.* 350 m Myr^{-1}. A small temperature increase (up to 20 ± 15 °C) of the upper part of the overlapped plate is explained by specific behaviour of steady-state geotherms calculated using lower radioactive heat production of metacarbonates as compared with metapelites. The suggested thermal-mechanical model corresponds well with *P–T* paths inferred from obtained thermobarometric data and correlates satisfactorily with *P–T* trajectories predicted by other two-dimensional thermal models for different crustal thickening and exhumation histories.

Key words: andalusite–kyanite phase transition, Fe- and Al-rich metapelites, tectono-thermal model, thermobarometry, Yenisey Ridge.

INTRODUCTION

In contrast to the progressive prograde transformation of andalusite- and/or kyanite-bearing to sillimanite-bearing assemblages common within low- and medium-pressure metamorphic complexes, the transformation from andalusite- to kyanite-bearing parageneses is unusual in orogenic belts. Normal 'static' continental geotherms do not cross the andalusite–kyanite stability curve (Kerrick, 1990), nor do the 'clockwise' *P–T* paths (P_{max} before T_{max}) typical for numerous collisional orogens (e.g. England & Richardson, 1977; Thompson & England, 1984; Dempster, 1985; Droop, 1985; Beaumont *et al.*, 2001; Jamieson *et al.*, 2002). Only a few examples for the transition of andalusite- to kyanite-bearing assemblages along a single prograde development are described in the literature, and these are attributed either to (1) metastable crystallization of andalusite in the kyanite stability field (Hollister, 1969), (2) pressure increase as a result of tectonic thickening by thrusting (Crawford & Mark, 1982; Baker, 1987; Clarke *et al.*, 1987; Beddoe-Stephens, 1990; Loosveld & Etheridge, 1990; Spear *et al.*, 1990, 2002; Ruppel & Hodges, 1994)

or (3) magma loading (Brown & Walker, 1993; Brown, 1996; Whitney *et al.*, 1999). *P–T* paths resulting from crustal thickening caused by thrusting or from pure-shear thickening differ distinctively from those predicted for magma loading (e.g. Jamieson *et al.*, 1998, 2002). In general, petrological analysis of mineral parageneses allows calculation of the *P–T* parameters and *P–T* paths of metamorphic rocks; microtextural relationships can then be used to fit these *P–T* data to sequences of structural events and, thus, to provide insight into the thermal and textural evolution of orogenic belts (e.g. Thompson & England, 1984). In this context this paper attempts to examine whether the *P–T* evolution of metamorphic rocks collected from the vicinity of a thrust fault and granitoid intrusion would record evidence of the thrust or magma emplacement.

Specifically the aims of the study are: (1) to describe the microtextures of rocks, with particular emphasis on the complex sequence of pseudomorphous replacement of andalusite and minerals in the adjacent matrix in order to distinguish conclusively between thrust fault-related and/or intrusion-related mineral parageneses, (2) to present the results of geothermobarometry and

P–T path calculations and (3) to discuss the implications of our results with respect to the tectonic and thermal evolution of the region.

GEOLOGICAL SETTING

The Yenisey Ridge occurs as a SW rim of the eastern Siberian platform (Fig. 1a). The Yenisey Ridge has a SSE–NNW extension of 700 by 150 km. The Transangarian region of the Yenisey Ridge comprises a Precambrian metamorphic terrane with an exposed extent of *c*. 450 by 150 km (Fig. 1b). According to Kornev (1986), it is composed of metamorphic complexes of different metamorphic grade separated by regional thrusts. The regional structural framework of the Transangarian Yenisey Ridge has traditionally
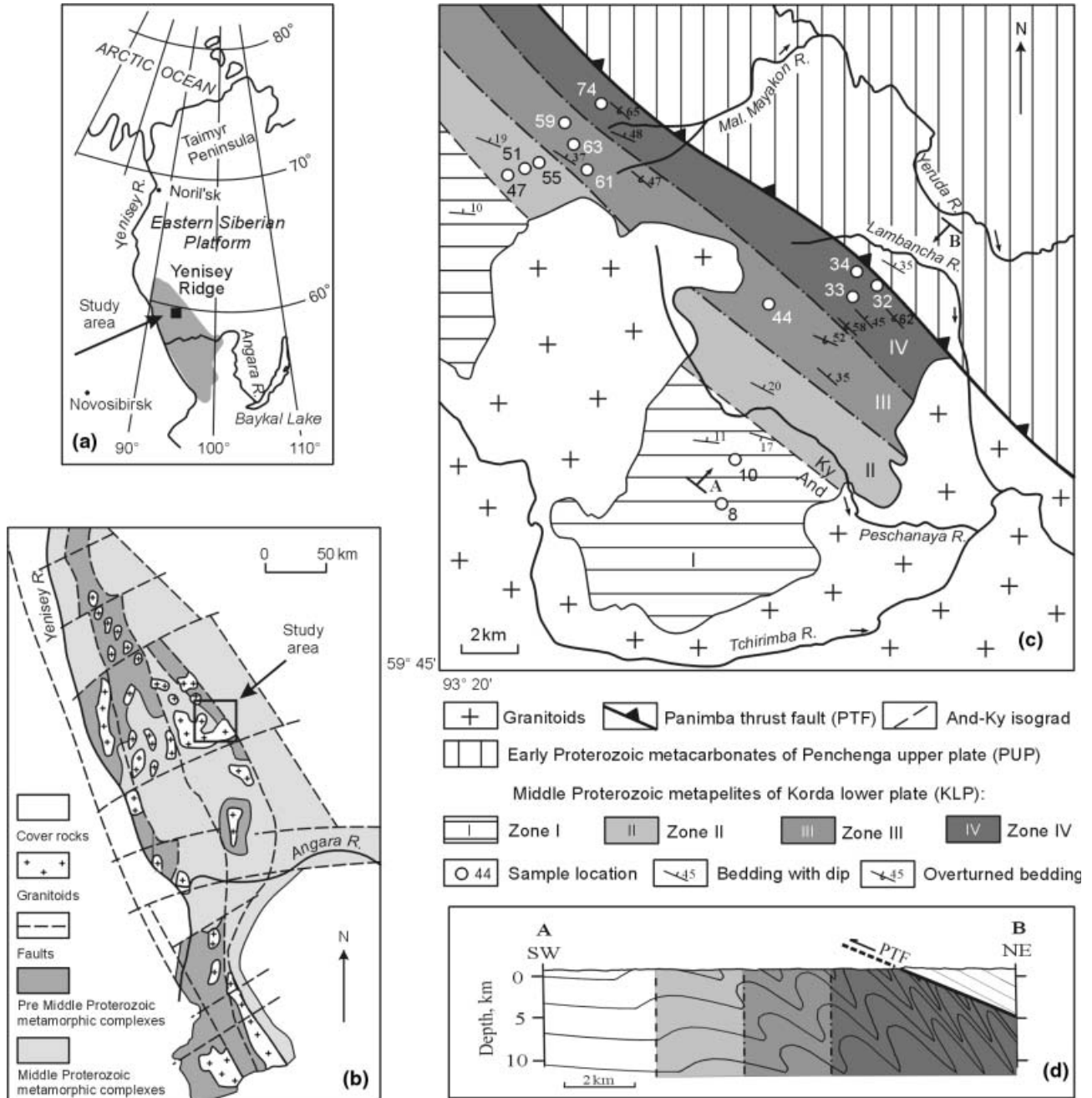

Fig. 1. (a) Location of the study area (the shaded area is the Yenisey Ridge); (b) general geological situation of the Yenisey Ridge; (c) geological sketch map of metamorphism at the eastern margin of the middle part of the Transangarian region in the vicinity of Panimba thrust and (d) schematic cross section across the Panimba thrust showing relative placement of metamorphic zones. A–B in (c) shows position of cross-section.

been interpreted as a system of NNW–SSE oriented crustal tectonic units (Fig. 1b), characterized by large-scale isoclinal folds dipping to the NE, accompanied by regionally developed schistosities; the thrusts follow the general structural trend of the Yenisey Ridge. According to structural and seismic data (Kozlov, 1994), the thrust systems generally are W-vergent dipping 40–60 ° to the NE.

At least two major Proterozoic events have been recognized by Postel'nikov (1990) and Khabarov (1994). The earlier (1400–850 Ma) event involved development of a thick (up to 10–12 km) continuous sequence of sedimentary rocks, which were formed as a result of consecutive accumulation of deep-water flysch sediments under subsidence of the basin floor of the Palaeoasian ocean. The latter (c. 850 Ma) event involved folding, thrusting along new and pre-existing faults and emplacement of granitoids during collisional orogenesis.

The study area is located between the Yeruda and Tchirimba Rivers at the eastern margin of the middle part of the Transangarian Yenisey Ridge (Fig. 1b). A schematic geological sketch map of this area (Fig. 1c) indicates two distinct tectonic units divided by a thrust zone. The Korda lower plate (KLP) is located SW of the Panimba thrust fault, tectonically underlying the early Proterozoic Penchenga upper plate (PUP) to the NE. The KLP represents regionally metamorphosed low-pressure, andalusite-bearing metapelites of middle Proterozoic age (1100 ± 50 Ma) that were overprinted by late Proterozoic (850 ± 50 Ma: K–Ar ages on biotite and muscovite; Dazenko, 1984; Zvyagina, 1989) medium-pressure kyanite-bearing assemblages and textures of regional metamorphism (Volobuev et al., 1968; Zvyagina, 1989). A sheet of medium-pressure rocks consists of an up to 7 km wide zone restricted in the NE by the Panimba thrust fault (Fig. 1c). The emplacement age of igneous rocks (granitoids on Fig. 1b) is also late Proterozoic, yielding Rb–Sr whole-rock ages of 850 ± 50 Ma (Dazenko, 1984), and correlating with the final stage of the medium-pressure overprint. Locally, these igneous rocks have also imparted a contact metamorphic overprint (Likhanov et al., 2001). These two late Proterozoic events may have occurred at approximately the same time.

Metamorphic zones and mineral assemblages

From c. 7–8 km to the southwest of the Panimba thrust fault (Fig. 1c), the degree of medium-pressure metamorphic overprint on the andalusite-bearing rocks and the intensity of deformation in the metapelites increase towards the fault (Likhanov et al., 2000). Four distinct metamorphic zones (Fig. 1c) in the KLP can be recognized. Rocks that are unaffected by the overprint comprise Zone I. The boundary between zones I and II coincides with the first appearance of kyanite towards the Panimba thrust fault. The other zone boundaries are related mainly to the style and

intensity of deformation, which mirror the progressive obliteration of an early microfabric characterized by an S1 axial planar foliation related to E-vergent D1 isoclinal folds. This foliation is dominant in the low-pressure, andalusite-bearing, middle Proterozoic–metamorphic rocks, where it is produced by preferred orientation of chlorite and mica. Superimposed on this early microfabric are subhorizontal D2 folds with an axial planar S2 crenulation cleavage that is weak in low-strain domains, but becomes more penetrative in higher-strain domains in the vicinity of the Panimba thrust. This new foliation represents the main regional fabric element in medium-pressure, kyanite-bearing rocks affected by the late Proterozoic overprint. Prominent structural features in the medium-pressure rocks are cataclastic deformation and boudinage.

Zone I

The rocks of the outermost Zone I typically consist of graphitic andalusite-bearing metapelites that were unaffected by medium-pressure metamorphism. The complex schistose fabric of these rocks displays microfolding, while the texture is porphyroblastic, with a lepidogranoblastic, medium-grained matrix that consists of recrystallized aggregates of muscovite–chlorite–biotite–plagioclase–quartz. The rocks are mainly characterised by And + Ms + Bt + Cld + Chl + Qtz ± Pl ± Crd mineral assemblages (Fig. 2; mineral abbreviations after Kretz, 1983). Assemblages of four and five 'AFM' minerals are confirmed where the constituent minerals are found close together or occur in several combination of two- and three-phase subassemblages within a single thin section. Idioblastic crystals of andalusite, up to 1.5 cm across, are fresh and locally pleochroic from colourless to pale pink or may be chiastolitic. In thin section, these crystals show hourglass growth structures indicated by graphite-bearing and graphite-free areas (Fig. 3a). Idioblastic prismatic and tabular crystals of chloritoid are commonly twinned (Fig. 3b). Quartz forms idioblastic as well as elongate and irregular grains up to 0.5 mm in diameter with straight and ovoid margins. Flakes of biotite, muscovite and chlorite up to 1 mm in length are the predominant matrix minerals that define the foliation in most rocks. Plagioclase is found as irregular grains or partly defines a foliation together with the phyllosilicates of the matrix. Laths of ilmenite as well as euhedral tabular chloritoid crystals (grain size: < 0.5 mm) also are oriented parallel to the foliation. Graphite is the most abundant minor mineral in all rocks. It usually occurs as small flakes up to 0.01 mm across, disseminated in the rock matrix. Cordierite occurs sporadically in massive and fine-grained hornfels with granoblastic texture within the narrow rim around granitoid intrusion. A likely possibility is that the cordierite-bearing assemblages in all zones was a product of contact metamorphism with the granitoid pluton.
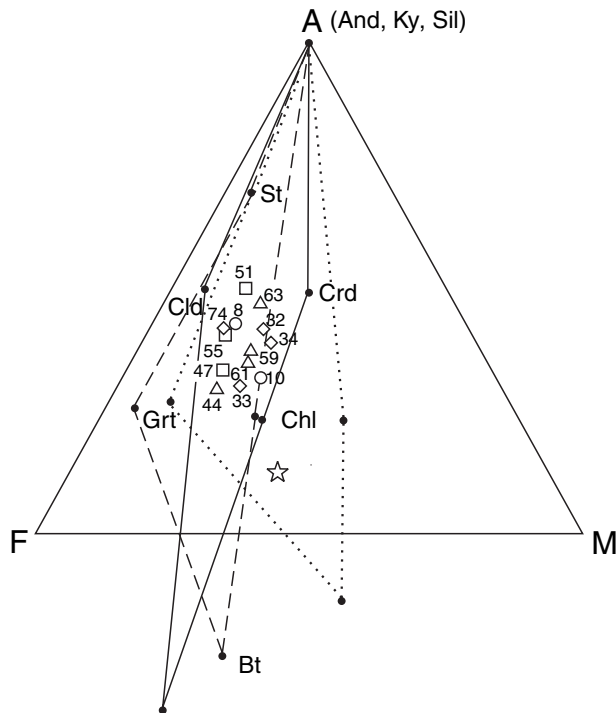
Fig. 2. AFM phase diagram (Thompson, 1957) representing typical mineral assemblages, drawn on the basis of representative phase compositions, as in Table 2. Open circles represent projected bulk compositions of samples from Zone I; squares, Zone II; triangles, Zone III; rhombuses, Zone IV as in Table 1. The star refers to the average low-grade pelite of Shaw (1956) and Symmes & Ferry (1992). Dots represent projected mineral compositions. Mineral compositions of Zone I are connected by solid lines; zones II–IV by dashed lines; and the more magnesian rocks of the Zone IV by dotted lines.

The first appearance of kyanite, defining the andalusite–kyanite isograd, marks the boundary between zones I and II. All rocks of zones II to IV are characterised by similar mineral assemblages (Fig. 2) and differ only in their degree and style of deformation. Their texture is porphyroblastic with a lepidogranoblastic, fine-grained matrix consisting of recrystallized aggregates of muscovite, chlorite, biotite, plagioclase, staurolite, quartz and garnet. Large pseudomorphs after andalusite are conspicuous in these samples. The centres of pseudomorphs are characterized by the assemblage kyanite + staurolite + muscovite + quartz (no garnet, chlorite, biotite, or plagioclase). Kyanite and andalusite are found only within the pseudomorphs and never occur in the matrix. Near the margins of the pseudomorphs, various assemblages locally containing eight or nine minerals may be found. They are represented by Ms + Bt + Chl + Qtz + Grt + St + Ky ± Pl ± Cld ± Sil ± And (relict) mineral assemblages (Fig. 2). The respective peak metamorphic assemblages of each zone grew syntectonically with S2, which is defined by phyllosilicates and ilmenite laths.

Zone II

Zone II rocks typically show cataclastic breaking of andalusite grains. Locally they are replaced by Kyn + St + Ms + Qtz pseudomorphs along fractures and margins (Fig. 3c). Macroscopically, andalusite porphyroblasts become grey and heterogeneous because of randomly oriented blades and radial sheaves of kyanite. The outline of the original andalusite crystals and the internal chiastolite inclusion pattern remain preserved. Two generations of staurolite crystals occur: large idioblastic porphyroblasts up to 1 mm and small crystals, 0.05–0.2 mm in length. The large porphyroblasts are characterised by vermicular quartz intergrowth textures concentrated at their rims (Giorgetti *et al.*, 2001). They also contain abundant small inclusions of chlorite and chloritoid. Muscovite flakes within the pseudomorphs are fine-grained randomly oriented aggregates. Garnet is also present as small idioblastic grains (0.1–1 mm across) only in the matrix, with abundant inclusions of ilmenite, muscovite, biotite, chloritoid and quartz. Biotite in the matrix exhibits kink-bands. At their rims, smaller fragments are rotated in the direction of the new foliation S2. The D1 fabric is sporadically overprinted by the younger D2 fabric. Towards Zone III, the modal amount of andalusite continues to decrease whereas that of garnet, kyanite and staurolite increase.

Zone III

This intermediate zone is characterized by more intensively deformed andalusite crystals, which are partially to totally replaced by Ky–St–Ms–Qtz pseudomorphs. Relict andalusite is rarely preserved in the cores of such pseudomorphs (Fig. 3d). In thin section, former square cross-sections take on a rhombic and ovoid habit. In proximity to granitoid intrusives the three polymorphs andalusite, kyanite and sillimanite have been found together (e.g. samples 44 & 61, Fig. 1c). Fibrous to rarely prismatic sillimanite crystals have grown at the margins of kyanite grains or along cleavages in andalusite crystals. Although all three aluminosilicate polymorphs are present in some samples, there is no evidence that they were ever in equilibrium. We infer that andalusite was the earliest one, whereas the relative timing of growth timing of kyanite and sillimanite is unclear. Texturally late fibrolitic sillimanite in the intermediate Zone III may have formed during an increase in temperature imposed by the intrusion (Likhanov *et al.*, 1998, 1999, 2001). In blastocataclasites, small garnet grains are disrupted by cracks and shifted along strain-slip cleavages. The fine-grained, mica-rich schistose matrix (average grain size of matrix minerals 0.1–1 mm) is deflected around the Ky–St–Ms–Qtz pseudomorphs after andalusite and locally wraps around garnet porphyroblasts.
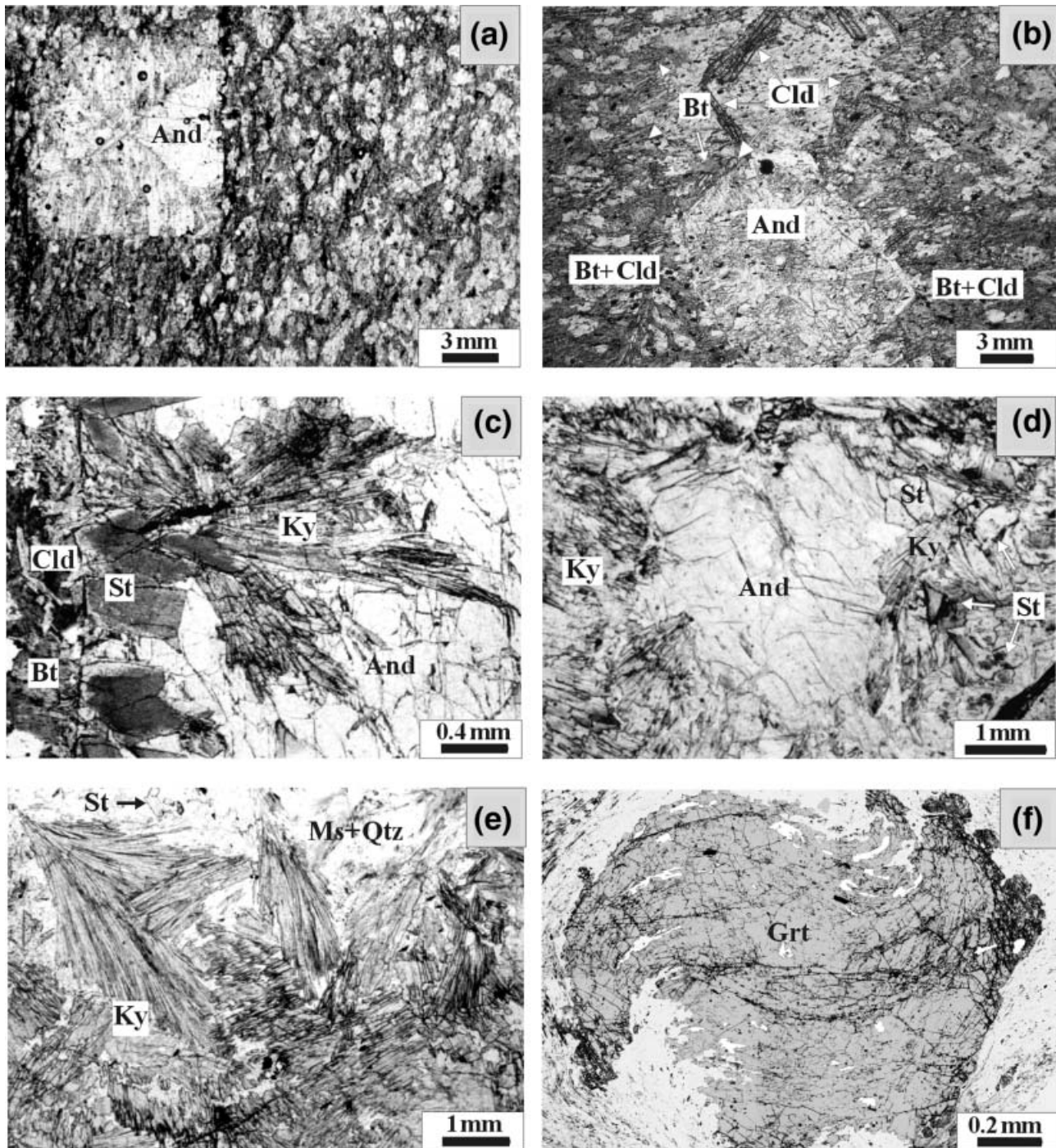
Fig. 3. Photomicrographs showing microtextural relationships among minerals in different zones of KLP: (a) idioblastic prismatic crystals of andalusite with hourglass growth structures and chloritoid porphyroblasts and (b) And + Cld + Bt assemblage in a quartz–plagioclase–chlorite–mica matrix in the Zone I; (c) early stage of pseudomorphous growth at the boundary between andalusite and biotite–chloritoid aggregates in the Zone II; (d) incomplete pseudomorphous replacement of andalusite by kyanite–staurolite–muscovite–quartz aggregates along grain margins in the Zone III; (e) complete replacement of andalusite; (f) garnet porphyroblasts containing smoothly curving spiral-shaped inclusion trails in the Zone IV.

Zone IV

As the Panimba thrust is approached, the last traces of relict andalusite disappear, marking the onset of the inner Zone IV (Fig. 3e). Here, adjacent to the Panimba thrust, the degree of deformation increases, resulting in the development of a linear mylonitic fabric contemporaneous with complete recrystallization of minerals

to form blastomylonites. The average grain size of the matrix minerals (0.01–0.1 mm) is usually smaller than that observed in other zones. All older structural features typical of zone I are completely obliterated. Ky–St–Ms–Qtz pseudomorphs after andalusite form lenses and layers parallel to S2. In some samples, these layers exhibit microboudinage, leading to the formation of lenses with recrystallized quartz invading the necks of these boudins. In contrast to the idioblastic garnet crystal in low-grade zones, garnet in zone IV forms lens-like porphyroblasts with well-developed strain shadows, reflecting growth under stress. This conclusion is supported by the shift of small garnet fragments along strain-slip cleavages and veins and lenses of granulated quartz. In some rocks garnet shows spiral-shaped inclusion fabrics (snowball structures) and sigmoidal patterns (Fig. 3f), which have traditionally been interpreted to result from the syntectonic growth of rotating porphyroblasts (e.g. Passchier & Trouw, 1996).

WHOLE-ROCK AND MINERAL CHEMISTRY

Whole-rock analyses were obtained by XRF, with the VRA-20 energy-dispersive spectrometer in the United Institute of Geology, Geophysics and Mineralogy, Novosibirsk. A selection of whole-rock data (Table 1) for metapelites from the four different zones reveals that the most prominent compositional difference among the samples involves weight percent variations in SiO_2 (57.14–62.59), Fe_2O_3 (6.36–12.87), Na_2O (0.29–1.13) and CaO (0.26–1.06). Such changes are probably related to local variations in the relative abundance of quartz-rich and extremely mica-rich layers within the samples, and in the modal amounts of plagioclase and carbonate. Average whole-rock data and standard deviations for metapelites from different zones were reported in previous work (Likhanov & Reverdatto, 2002). These data reveal that these rocks have a nearly identical composition (overlap within errors) for all major elements. Although negligible compositional differences in element concentration among the samples involving variations in FeO and MgO exist, they are not systematically related to metamorphic grade. The unaltered rocks of zone I (protoliths) and their altered equivalents of zones II–IV are homogeneous metapelites with a narrow range of high Fe- [X_{Fe} = FeO/(FeO + MgO + MnO) = 0.68–0.69 whole rock on a mole basis] and high Al- [X_{Al} = Al_2O_3–3K_2O/(Al_2O_3–3K_2O + FeO + MgO + MnO) = 0.38–0.41] bulk compositions as compared with the average pelite whole-rock compositions (X_{Fe} = 0.52 and X_{Al} =

0.13) (Shaw, 1956; Symmes & Ferry, 1992) and plot above the garnet–chlorite tie-line in the AFM projection of Thompson in Fig. 2. The bulk-rock Mn-content of the pelitic schists [X_{Mn} = MnO/(MnO + FeO + MgO)] varies from 0.01 to 0.03, consistent with the whole-rock MnO content of normal pelitic schists (Grambling, 1986). Compared with the average pelitic rock compositions of Ague (1991), the rocks investigated here are more depleted in K_2O, CaO and Na_2O.

Chemical analyses of all minerals in the metapelites were obtained with an X-ray EDAX DX-4 attached to a SEM Philips XL-30 at the University of Siena, and with electron microprobes at the Institute of Mineralogy and Petrography, Novosibirsk (Camebax; Cameca Instruments, Courbevoie, France) as well as the Ruhr-University of Bochum (Cameca SX-50). Operating parameters were: 10 nA (Bochum), 40 nA (Novosibirsk), and 50 nA (Siena) beam current; 15 kV (Bochum), 20 kV (Siena, Novosibirsk) accelerating voltage; 20 s (Novosibirsk, Bochum), 100 s (Siena) counting time for all elements and an electron beam diameter of 3–4 μm. PAP (Novosibirsk, Bochum) and ZAF (Siena) corrections were applied to the data. Representative analyses are given in Table 2. Garnet was analysed by making a traverse across a grain with an analysis at least every 15 μm, depending on the size of the grain. The presence of graphite and nearly pure ilmenite in every rock indicates that the oxidation ratio was low and that Fe^{3+} should be minor (Holdaway *et al.*, 1988).

Andalusite, kyanite and *sillimanite* are pure Al_2SiO_5 within detection limits of the electron microprobe, and thus must have low Fe contents of <0.01 atoms per formula unit.

Garnet compositions are essentially in the range of Alm_{83-85}, Prp_{7-8}, Sps_{4-7}, Grs_{2-4} with X_{Fe} values in the narrow range 0.91–0.92. There is weak normal growth zoning (Table 2), as shown by the representative core-rim analyses of sample 61 from Zone III (Fig. 4): $Alm_{83.4}$, $Prp_{8.1}$, $Sps_{6.3}$, $Grs_{2.2}$ at the core to $Alm_{83.9}$, $Prp_{8.3}$, $Sps_{4.7}$, $Grs_{3.1}$ at the inner rim ('inner rim' is defined as the zone not affected by late-stage diffusion). Generally, garnet is characterized by a slight increase of grossular component and a decrease of spessartine component from core to rim, and by a conspicuously flat zoning profile with nearly constant X_{Fe} (Table 2; Fig. 4). An exception is garnet from the more magnesian rocks of the inner zone IV (samples 32 & 34, Fig. 4) which show an increase in grossular component and a slight decrease in spessartine, almandine and pyrope components from core to rim, with nearly constant X_{Fe} (0.83–0.84).

Staurolite compositions are very similar in all analysed samples. MnO and ZnO contents are very low and vary only slightly (0.11–0.16 and 0.92–0.99 wt%, respectively). The staurolite is relatively unzoned and shows lower X_{Fe} values (0.87) than coexisting garnet.

Biotite is unzoned, and the composition of biotite grains in contact with garnet (also as inclusions) does not differ significantly from the composition in grains away from garnet. The tetrahedral Al-content increases slightly from zone I to zones II–IV (1.04–1.07 to 1.25–1.34 p.f.u.), whereas X_{Fe} values decrease (from 0.69 in

Table 1. Whole-rock major element data for metapelitic rocks from the four different metamorphic zones.

Zone:	I		II			III				IV			
	8	10	47	51	55	44	59	61	63	32	33	34	74
Sample													
SiO_2	58.32	62.59	60.22	58.40	57.25	57.81	59.71	61.09	57.17	58.14	60.98	58.59	57.14
TiO_2	0.86	0.95	0.94	1.15	1.06	0.81	0.96	0.92	0.95	0.96	0.95	0.58	0.86
Al_2O_3	21.47	18.28	19.06	22.89	21.30	19.33	20.43	19.17	24.69	23.06	19.60	21.68	22.66
Fe_2O_3	8.29	8.64	10.30	6.36	9.15	12.87	7.48	7.41	7.96	9.80	8.19	9.01	9.63
MnO	0.07	0.07	0.11	0.17	0.25	0.12	0.03	0.05	0.05	0.11	0.09	0.15	0.04
MgO	1.54	2.81	1.92	1.19	1.53	2.36	1.89	1.89	2.03	1.99	1.99	2.81	1.52
CaO	0.23	0.20	0.24	0.97	0.34	0.42	0.27	0.20	0.31	0.25	0.26	1.06	0.31
Na_2O	0.3	0.29	0.31	0.92	1.13	0.32	0.48	0.48	0.48	0.72	0.72	0.3	0.29
K_2O	3.24	2.91	3.08	3.38	3.29	3.03	3.01	3.52	2.52	3.44	3.97	2.12	2.67
LOI	5.29	2.61	3.79	3.86	4.58	2.69	4.83	4.81	2.94	1.90	2.54	2.73	4.87
Total	99.61	99.35	99.97	99.29	99.88	99.76	99.09	99.54	99.10	100.3	99.29	99.03	99.99

Total iron as Fe_2O_3.
LOI, loss on ignition.

Table 2. Representative mineral analyses and structural formulae.

Garnet

Zone	II			III						IV					
Sample	55 rim	47 rim	51 rim	59 rim	63 rim	44 core	44 rim	61 core	61 rim	32 rim	33 rim	34 core	34 rim	74 core	74 rim
SiO_2	36.78	36.82	36.74	36.25	36.41	36.29	36.22	36.14	36.26	37.40	36.83	36.88	37.40	36.05	36.11
TiO_2	0.10	0.09	0.08	0.08	0.09	0.03	0.04	0.02	0.04	0.00	0.04	0.00	0.00	0.03	0.04
Al_2O_3	20.14	20.18	20.08	20.43	20.37	20.32	20.26	20.30	20.23	21.01	20.04	20.79	20.96	20.21	20.12
FeO	38.37	38.24	38.38	38.41	38.27	38.15	38.14	37.97	38.25	33.48	38.23	33.67	33.62	38.21	38.34
MnO	2.11	2.13	2.27	2.14	2.21	2.88	2.31	2.88	2.16	0.64	2.40	0.95	0.66	3.17	2.16
MgO	1.96	1.93	1.92	1.97	1.96	2.13	2.21	2.05	2.13	3.08	1.91	3.77	3.54	2.04	1.98
CaO	0.88	0.85	0.90	1.11	1.14	0.68	1.03	0.79	1.14	4.12	1.53	2.02	3.81	0.80	1.55
Total	100.3	100.2	100.4	100.4	100.5	100.4	100.2	100.2	100.2	99.73	100.9	99.08	99.99	100.3	100.3
Cations per 12 oxygen															
Si	3.00	3.01	3.00	2.96	2.97	2.96	2.96	2.96	2.97	2.99	2.99	3.01	2.99	2.96	2.96
Ti	0.01	0.01	0.01	0.01	0.01	0.00	0.00	0.00	0.00	0.00	0.00	0.00	0.00	0.00	0.00
Al	1.94	1.94	1.93	1.97	1.96	1.96	1.95	1.96	1.95	1.99	1.92	2.00	1.98	1.95	1.95
Fe	2.62	2.61	2.62	2.63	2.61	2.61	2.61	2.60	2.62	2.25	2.60	2.30	2.25	2.62	2.63
Mn	0.15	0.15	0.16	0.15	0.15	0.20	0.16	0.20	0.15	0.06	0.17	0.07	0.04	0.22	0.15
Mg	0.24	0.23	0.23	0.24	0.24	0.26	0.27	0.25	0.26	0.38	0.23	0.46	0.42	0.25	0.24
Ca	0.08	0.07	0.08	0.10	0.10	0.06	0.09	0.07	0.10	0.34	0.13	0.18	0.33	0.07	0.14
X_{Alm}	0.850	0.851	0.848	0.844	0.842	0.834	0.835	0.834	0.839	0.743	0.831	0.766	0.740	0.830	0.833
X_{Sps}	0.047	0.048	0.051	0.048	0.049	0.062	0.051	0.063	0.047	0.019	0.052	0.022	0.013	0.069	0.047
X_{Prp}	0.077	0.077	0.076	0.077	0.077	0.083	0.084	0.081	0.083	0.126	0.074	0.153	0.138	0.079	0.077
X_{Grs}	0.026	0.024	0.025	0.031	0.032	0.021	0.030	0.022	0.031	0.113	0.042	0.059	0.109	0.022	0.043

Plagioclase

Zone	I		II			III				IV				
Sample	8 rim	10 rim	55 rim	47 rim	51 rim	59 rim	63 rim	44 rim	61 rim	32 rim	33 rim	34 core	34 rim	74 rim
SiO_2	65.76	65.67	64.81	64.91	64.72	64.53	64.98	65.01	64.88	57.64	65.05	56.80	59.67	64.91
Al_2O_3	21.45	21.57	22.18	22.23	22.18	22.68	22.08	21.99	21.92	25.81	22.24	26.51	24.81	22.12
FeO	0.20	0.14	0.00	0.05	0.06	0.14	0.11	0.00	0.05	0.08	0.00	0.03	0.11	0.12
CaO	1.28	1.99	2.40	2.43	2.41	2.29	2.40	2.44	2.41	8.36	2.45	9.15	7.25	2.41
Na_2O	10.47	10.23	9.61	9.57	9.63	9.42	9.38	9.61	9.50	7.24	9.53	6.84	7.96	9.62
K_2O	0.07	0.06	0.29	0.30	0.25	0.24	0.18	0.27	0.24	0.06	0.34	0.10	0.05	0.15
Total	99.23	99.66	99.29	99.49	99.25	99.30	99.13	99.32	99.00	99.19	99.61	99.43	99.85	99.33
Cations per 8 oxygen														
Si	2.90	2.89	2.87	2.86	2.86	2.85	2.87	2.87	2.87	2.61	2.87	2.57	2.67	2.87
Al	1.12	1.12	1.16	1.16	1.16	1.18	1.15	1.15	1.14	1.38	1.16	1.41	1.31	1.15
Fe	0.01	0.01	0.00	0.00	0.00	0.01	0.00	0.00	0.00	0.00	0.00	0.00	0.00	0.00
Ca	0.06	0.09	0.11	0.12	0.11	0.11	0.11	0.12	0.11	0.405	0.12	0.44	0.35	0.11
Na	0.90	0.87	0.82	0.82	0.83	0.81	0.80	0.82	0.82	0.634	0.81	0.60	0.69	0.82
K	0.00	0.00	0.02	0.02	0.01	0.01	0.01	0.02	0.01	0.00	0.02	0.01	0.00	0.00
X_{An}	0.063	0.094	0.119	0.121	0.119	0.116	0.124	0.121	0.122	0.389	0.122	0.420	0.334	0.121

Biotite

Zone	I		II			III				IV			
Sample	8	10	55	47	51	59	63	44	61	32	33	34	74
SiO_2	34.92	34.52	34.80	34.82	34.62	34.75	34.61	34.74	34.46	36.94	34.70	37.14	34.75
TiO_2	1.84	1.99	3.00	2.91	2.87	3.05	2.76	2.62	2.69	1.62	3.10	1.38	2.76
Al_2O_3	18.87	19.22	19.06	19.11	19.17	19.15	19.09	19.05	19.40	19.41	18.87	19.32	19.22
FeO	23.91	24.98	22.22	22.36	22.41	22.14	22.43	22.35	21.97	17.28	22.28	16.92	22.43
MnO	0.09	0.16	0.08	0.10	0.08	0.10	0.13	0.04	0.09	0.09	0.10	0.08	0.07
MgO	6.01	6.15	7.24	7.48	7.34	7.33	7.37	7.65	7.37	11.82	7.45	12.08	7.39
Na_2O	0.18	0.14	0.19	0.16	0.15	0.20	0.18	0.19	0.18	0.28	0.14	0.53	0.17
K_2O	9.84	8.16	8.69	9.02	8.99	8.99	8.84	8.73	9.08	8.14	9.03	7.98	8.91
Total	95.66	95.32	95.28	95.96	95.63	95.71	95.41	95.37	95.24	95.58	95.67	95.43	95.70
Cations per 11 oxygen													
Si	2.96	2.93	2.68	2.67	2.66	2.67	2.67	2.67	2.66	2.74	2.67	2.75	2.67
Ti	0.12	0.13	0.17	0.17	0.17	0.18	0.16	0.15	0.16	0.09	0.18	0.08	0.16
Al^{IV}	1.04	1.07	1.32	1.33	1.34	1.33	1.33	1.33	1.34	1.26	1.33	1.25	1.33
Al^{VI}	0.85	0.85	0.41	0.40	0.40	0.40	0.40	0.40	0.42	0.44	0.38	0.44	0.41
Fe	1.70	1.77	1.43	1.43	1.44	1.42	1.45	1.44	1.42	1.07	1.43	1.05	1.44
Mn	0.01	0.01	0.01	0.01	0.01	0.01	0.01	0.00	0.01	0.01	0.01	0.01	0.01
Mg	0.76	0.78	0.83	0.85	0.84	0.84	0.85	0.88	0.85	1.31	0.85	1.33	0.85
Na	0.03	0.02	0.03	0.02	0.02	0.03	0.03	0.03	0.03	0.04	0.02	0.08	0.03
K	1.07	0.88	0.85	0.88	0.88	0.88	0.87	0.86	0.89	0.77	0.89	0.75	0.87
X_{Fe}	0.691	0.694	0.633	0.601	0.632	0.628	0.630	0.621	0.626	0.450	0.627	0.441	0.629

Table 2. (*Cont'd*).

	Muscovite												
Zone	I		II			III				IV			
Sample	8	10	55	47	51	59	63	44	61	32	33	34	74
SiO_2	45.91	47.67	45.42	46.38	46.46	45.94	46.00	45.32	45.30	47.17	44.97	47.37	45.38
TiO_2	0.55	0.23	0.62	0.25	0.26	0.54	0.51	0.65	0.52	0.29	0.54	0.48	0.60
Al_2O_3	35.98	35.85	35.85	36.75	36.56	35.96	36.36	36.21	35.28	35.86	35.37	35.33	36.51
FeO	1.03	0.72	1.35	0.93	1.04	1.06	1.27	1.49	1.75	0.66	1.78	0.87	1.23
MgO	0.58	0.39	0.58	0.39	0.48	0.63	0.59	0.53	0.68	0.82	0.61	1.20	0.51
Na_2O	0.71	0.55	0.73	1.96	1.37	0.72	0.78	0.60	0.68	0.70	0.74	1.03	0.91
K_2O	10.46	8.94	10.11	8.64	9.20	10.24	10.33	10.58	10.08	9.46	10.09	8.66	10.05
Total	95.22	94.35	94.66	95.30	94.37	95.09	95.84	95.38	94.29	94.96	94.10	94.94	95.19
Cations per 11 oxygen													
Si	3.05	3.15	3.04	3.06	3.07	3.06	3.04	3.02	3.04	3.11	3.04	3.12	3.02
Ti	0.03	0.01	0.03	0.01	0.01	0.03	0.03	0.03	0.03	0.02	0.03	0.03	0.03
Al^{IV}	0.95	0.85	0.96	0.94	0.93	0.94	0.96	0.98	0.96	0.89	0.96	0.88	0.98
Al^{VI}	1.87	1.94	1.87	1.91	1.91	1.88	1.87	1.86	1.87	1.90	1.86	1.87	1.88
Fe	0.06	0.04	0.08	0.05	0.06	0.06	0.07	0.08	0.08	0.04	0.10	0.05	0.07
Mg	0.06	0.04	0.06	0.04	0.05	0.06	0.06	0.05	0.06	0.08	0.06	0.12	0.05
Na	0.09	0.07	0.10	0.25	0.18	0.09	0.10	0.08	0.10	0.09	0.10	0.13	0.12
K	0.89	0.75	0.86	0.73	0.77	0.87	0.87	0.90	0.86	0.80	0.87	0.73	0.85
X_{Na}	0.092	0.085	0.104	0.255	0.189	0.094	0.103	0.082	0.104	0.101	0.103	0.151	0.123

	Chlorite				Chloritoid		Staurolite		Ilm	And	Ky	Sil	Crd	Mrg	Tur
Zone	I		II	IV	I	III	II	IV	II	III	IV	III	I	I	IV
Sample	8	10	55	74	8	63	55	74	51	63	33	44	10	10	33
SiO_2	23.01	24.37	22.79	23.34	24.14	23.88	26.99	27.37	0.03	36.36	36.42	36.33	48.32	30.01	36.87
TiO_2	0.14	0.04	0.24	0.16	0.00	0.01	0.04	0.08	53.79	0.00	0.02	0.05	0.04	0.04	0.69
Al_2O_3	21.72	22.52	21.72	22.63	40.48	40.67	54.26	54.43	0.03	63.52	63.38	63.12	30.86	50.61	34.16
FeO	30.00	29.92	30.54	31.09	25.33	24.97	14.48	14.64	44.40	0.23	0.22	0.37	11.27	0.42	9.19
MnO	0.12	0.10	0.08	0.06	0.28	0.29	0.16	0.11	0.79	0.02	0.00	0.01	0.19	0.04	0.01
MgO	10.85	10.75	10.54	10.62	2.13	1.98	1.17	1.19	0.04	0.00	0.04	0.08	6.18	0.13	4.47
CaO	0.00	0.00	0.02	0.00	0.00	0.01	0.00	0.03	0.00	0.00	0.00	0.02	0.03	12.37	0.19
Na_2O	0.11	0.00	0.12	0.04	0.05	0.00	0.00	0.00	0.00	0.02	0.02	0.03	0.77	0.93	1.56
K_2O	0.05	0.00	0.03	0.03	0.00	0.03	0.00	0.01	0.00	0.02	0.00	0.03	0.00	0.02	0.08
ZnO	0.00	0.00	0.00	0.00	0.06	0.09	0.99	0.92	0.00	0.00	0.00	0.00	0.00	0.00	0.03
Total	86.00	87.70	86.08	87.97	92.47	91.93	98.09	98.78	99.08	100.2	100.1	100.1	97.66	94.57	87.30
	Cations per 14 oxygen				12(O)		48(O)		3(O)	Cations per 5 oxygen			18(O)	11(O)	31(O)
Si	2.55	2.63	2.53	2.54	2.01	1.99	7.87	7.92	0.00	0.98	0.98	0.98	5.09	2.01	6.21
Ti	0.01	0.00	0.02	0.01	0.00	0.00	0.01	0.02	1.02	0.00	0.00	0.00	0.00	0.00	0.09
Al	2.84	2.87	2.86	2.90	3.96	4.00	18.63	18.56	0.00	2.02	2.02	2.01	3.83	3.99	6.78
Fe	2.78	2.70	2.84	2.82	1.76	1.74	3.53	3.54	0.94	0.01	0.01	0.01	0.99	0.02	1.29
Mn	0.01	0.01	0.01	0.01	0.02	0.02	0.04	0.03	0.02	0.00	0.00	0.00	0.02	0.00	0.00
Mg	1.79	1.73	1.75	1.72	0.26	0.25	0.51	0.51	0.00	0.00	0.00	0.00	0.97	0.01	1.12
Ca	0.00	0.00	0.00	0.00	0.00	0.00	0.00	0.01	0.00	0.00	0.00	0.00	0.00	0.89	0.03
Na	0.02	0.00	0.03	0.01	0.01	0.00	0.00	0.00	0.00	0.00	0.00	0.00	0.16	0.12	0.51
K	0.01	0.00	0.00	0.00	0.00	0.00	0.00	0.00	0.00	0.00	0.00	0.00	0.00	0.00	0.01
Zn	0.00	0.00	0.00	0.00	0.00	0.01	0.21	0.20	0.00	0.00	0.00	0.00	0.00	0.00	0.01
X_{Fe}	0.608	0.609	0.619	0.621	0.874	0.875	0.873	0.874					0.505		0.535

$X_{Alm} = Fe/(Fe + Mg + Mn + Ca)$, $X_{Prp} = Mg/(Fe + Mg + Mn + Ca)$, $X_{Sps} = Mn/(Fe + Mg + Mn + Ca)$, $X_{Grs} = Ca/(Fe + Mg + Mn + Ca)$, $X_{An} = Ca/(Ca + Na + K)$,
$X_{Fe} = Fe/(Fe + Mg)$ and $X_{Na} = Na/(Na + K)$.
Total Fe expressed as FeO.
0.00 means below detection limits.

zone I to 0.60–0.44 p.f.u. in zones II–IV). The most magnesium biotite ($X_{Fe} = 0.44$–0.45) occurs in the inner zone IV (samples 32 and 34).

White mica varies in celadonite content (expressed as the $(Mg + Fe)/(Mg + Fe + Al^{VI})$ ratio) from 0.08 to 0.16, in paragonite (X_{Na}) content from 0.085 to 0.255; and in Si-content from 3.02 to 3.15 p.f.u. There are no significant differences in muscovite composition between decussate muscovite inside the Ky–St–Ms–Qtz pseudomorphs and muscovite in the matrix.

Plagioclase shows a slight increase of the anorthite component from albite ($X_{An} = 0.06$–0.09) in zone I to oligoclase ($X_{An} = 0.12$) in zones II–IV. In two samples (32 and 34) of the inner zone IV, an abrupt increase of anorthite component to sodic andesine occurs. Here, plagioclase is commonly zoned, with the core slightly more anorthitic ($X_{An} = 0.42$) than the rim ($X_{An} = 0.33$).

Chlorite is chemically homogeneous in each sample, with similar X_{Fe} in the narrow range of 0.61–0.62. As an exception, chlorite of sample 34 exhibits an X_{Fe} ratio of *c.* 0.41.

Chloritoid is chemically homogeneous and remarkably iron-rich, with X_{Fe} in the narrow range of 0.871–0.874.

Ilmenite in all samples is close to its ideal end-member composition, with constant amounts of Mn (0.02 atoms p.f.u.).

Margarite contains low amounts of paragonite component, typically $Mrg_{88}Pg_{12}$.

Tourmaline is aluminous schorl-dravite with $X_{Fe} = 0.535$.

All samples contain low amounts of *calcite* with low FeO contents (2.76 wt%).

One of the samples analysed from the andalusite-bearing rocks of the Zone I contains *cordierite*. This cordierite is chemically homogeneous with Na_2O contents of *c.* 0.77 wt% and X_{Fe} of 0.505.
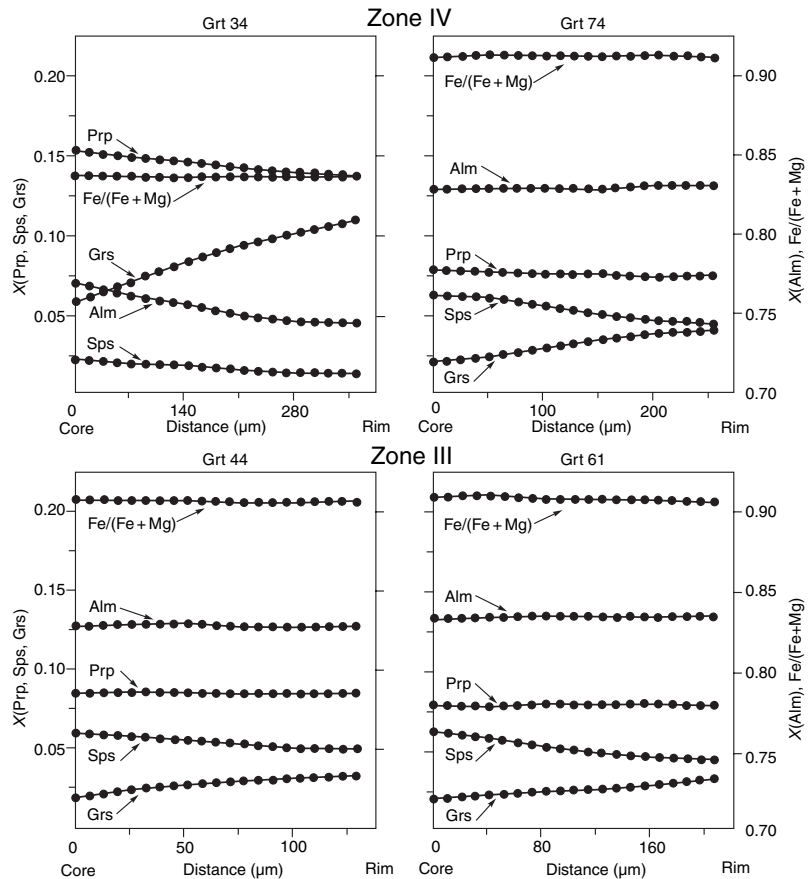
Fig. 4. Compositional zoning profiles across garnet crystals from samples of III and IV zones.

Metamorphic conditions

There are two basic approaches to quantitative geothermobarometry of metamorphic rocks. The first is conventional 'absolute' thermobarometry, which focuses on determination of the pressure and temperature conditions at which a rock equilibrated at some point in its history. A second approach 'relative' thermobarometry is exemplified by the determination of changes in physical conditions experienced by a rock through analysis of mineral zoning and reaction microtextures (Spear, 1989).

'Absolute' thermobarometry

Metamorphic conditions for metapelites from the four different zones were deduced on the basis of pressure estimates obtained from net transfer equilibria and estimates of metamorphic temperatures obtained from exchange thermometers (Table 3). Temperature estimates for Zone I rocks were obtained using three geothermometers involving the minerals Bt–Cld (Perchuk, 1991), Bt–Ms (Hoisch, 1989) and Chl–Cld (Vidal *et al.*, 1999). Two modifications of the Bt–Ms–Chl geobarometer (Powell & Evans, 1983; Bucher-Nurminen, 1987) were used to determine pressures. Temperature estimates of garnet-bearing rocks of Zones II–IV were

obtained using garnet-biotite geothermometers and the calibrations of: (1) Ferry & Spear (1978), with appropriate mixing models of Hodges & Spear (1982), (2) Kleemann & Reinhardt (1994), (3) Perchuk & Lavrent'eva (1983) and (4) Holdaway *et al.* (1997). For this purpose, rim analyses of 11 garnet–biotite pairs were combined from thin-section domains in which these minerals were not in actual physical contact. The two modifications of the Grt–Bt–Ms–Pl geobarometers of Ghent & Stout (1981) and Hoisch (1990) were used to determine pressures using garnet rim compositions, neighbouring biotite, muscovite and plagioclase. Equilibria involving the Al_2SiO_5–Grt–Pl–Qtz were not employed for pressure estimates, as noted by Essene (1989), the accuracy and precision of pressures determined from these equilibria are generally poor in metamorphic terranes with coexistence of a few aluminosilicates. The calibration of Ghent & Stout (1981) was combined activity–composition models of Hodges & Crowley (1985) for ideal solid solution of biotite and non-ideal solution of garnet, plagioclase and muscovite. Hoisch (1991) involves non-ideal solutions of garnet and plagioclase, and non-ideality in the mixing of cations on the octahedral sites of muscovite and biotite. For each thin-section domain considered, a *P–T* estimate was calculated by simultaneous solution of these equilibria. The results are summarized in Table 3 and in Fig. 5.

	T (°C)								P (kbar)				
	1	2	3	4	5	6	7	8	9	10	11	12	8
Zone I													
8					542	549	551				3.8–4.0	3.5–3.9	
10							562	553 ± 22			3.7	3.6	3.3 ± 0.7
Zone II													
47	538	560	561	568					4.63 ± 0.44	4.54			
51	537	561	559	573					4.83 ± 0.41	4.66			
55	547	562	566	570				572 ± 13	5.05 ± 0.32	4.85			4.6 ± 0.2
Zone III													
63	552	567	566	582				568 ± 18	5.65 ± 0.46	5.73			4.8 ± 1.0
61	571	574	589	598				571 ± 14	5.97 ± 0.29	5.73			5.2 ± 0.3
44	569	577	593	601					5.87 ± 0.34	5.77			
59	549	565	568	580				567 ± 16	5.75 ± 0.36	5.92			5.6 ± 0.9
Zone IV													
33	544	564	569	572					6.22 ± 0.29	6.20			
32	550	567	570						6.30 ± 0.28	6.29			
34	540	572	568					632 ± 40	6.38 ± 0.34	6.42			7.6 ± 1.2
74	563	570	579	584				572 ± 16	6.68 ± 0.45	6.70			5.9 ± 0.9

Table 3. Summary of pressure and temperature estimates using conventional barometers and thermometers and the average *P–T* approach of Powell & Holland (1994) for selected samples.

1, Grt–Bt geothermometer (Ferry & Spear, 1978); 2, Grt–Bt geothermometer (Kleemann & Reinhardt, 1994); 3, Grt–Bt geothermometer (Perchuk & Lavrent'eva, 1983); 4, Grt–Bt geothermometer (Holdaway *et al.*, 1997); 5, Bt–Cld geothermometer (Perchuk, 1991); 6, Chl–Cld geothermometer (Vidal *et al.*, 1999); 7, Bt–Ms geothermometer (Hoisch, 1989); 8, THERMOCALC calculations (Powell & Holland, 1994); 9, Grt–Bt–Ms–Pl geobarometer (Ghent & Stout, 1981) with calculated uncertainties in pressure estimates; 10, Grt–Bt–Ms–Pl geobarometer (Hoisch, 1990); 11, Bt–Ms–Chl geobarometer (Powell & Evans, 1983); 12, Bt–Ms–Chl geobarometer (Bucher-Nurminen, 1987).
The results of the average *P–T* calculations made using the computer software THERMOCALC are shown with ± 2σ errors.

These data suggest a progressive pressure increase toward the Panimba thrust from 3.5–4 kbar in Zone I to 4.5–5 and 5.5–6 kbar in zones II and III, respectively, to 6.2–6.7 kbar in Zone IV. As the Panimba thrust is approached, the mean maximum temperatures increase only slightly from 560 to 580 °C, indicating a surprisingly low geothermal gradient of 1–7 °C km^{-1} during the late Proterozoic metamorphic overprint. The maximum recorded temperatures of almost 600 °C are noted for the two sillimanite-bearing mineral assemblages of samples 61 and 44, which are located in the intermediate Zone III adjacent to granite intrusive. A likely possibility is that these sillimanite-bearing assemblages may have been influenced by contact metamorphism around the granitoid intrusive (Likhanov *et al.*, 1998, 1999, 2001).

To test the reliability of these *P–T* estimates, the same analytical and assemblage data were processed with the average *P–T* method, using the computer software THERMOCALC (Powell & Holland, 1994) with the internally consistent thermodynamic dataset of Holland & Powell (1990) (Table 3). The activities of the end-member components of the analysed minerals were calculated using the activity–composition relations suggested by Holland & Powell (1990, 1998). The *P–T* conditions inferred from the THERMOCALC calculations are generally in good agreement with the *P–T* conditions estimated from conventional thermobarometry, except the pressure estimates for samples 63 from zone III and 74 from zone IV. Taking into account the uncertainties at a 2σ level, error estimates for the THERMOCALC method substantially overlap the values quoted for zones III and II. This difference in pressure estimates between the various methods are the product of both differences in thermodynamic data

sets and of the fact that the THERMOCALC method considers all the end-member phases presented when calculating *P–T*, rather than just the end-members involved in specific geothermometers and geobarometers, and thus is less prone to the problems associated with a specific geothermobarometer (Powell & Holland, 1988).

As the *P–T* range for equilibration of the samples from adjacent zones may be partially overlapped, the accuracy of *P–T* estimates needs to be evaluated. Geobarometry is generally less precise than geothermometry (Essene, 1989), and the uncertainties involved can be considered in terms of overall and comparison uncertainties (Hodges & McKenna, 1987). Overall uncertainties incorporate all the systematic (e.g. thermodynamic data and activity–composition relations) and random (e.g. mineral composition and microprobe analysis) uncertainties and are appropriate when absolute pressure estimates are being sought. Comparison uncertainties only involve the random uncertainties (i.e. compositional data) and are appropriate if relative differences in pressure are sought. Specifically, if a single barometer is used to calculate differences in pressure, then any calibration uncertainties cancel each other out, and the differences in pressure of equilibration can be calculated by considering only the effects of analytical errors and errors in a reaction enthalpy (Spear, 1993). A magnitude of the errors resulting from the above assumptions have been computed by error propagation of analytical imprecision in microprobe analysis for major and minor elements by using the calculations obtained from the basic error propagation equation (Spear, 1993) and the combined differential method of estimating uncertainties (Taubert, 1988). All calculations were per-
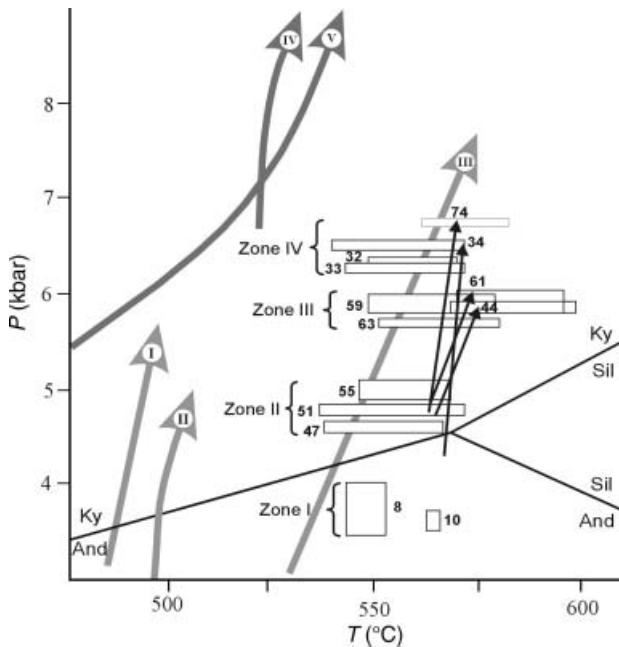
Fig. 5. *P–T* diagram summarizing the results of pressure and temperature as well as *P–T* path calculations for KLP rocks SW of the Panimba thrust and for other overthrust terranes. Each rectangle represents *P–T* estimates calculated from various geothermobarometers from the same sample. The generalized *P–T* paths derived from compositional zoning in garnet and correlated garnet and plagioclase compositions are shown by black thin arrows in the core-to-rim direction; the position of the arrow head indicates the sample number. Arrow head on other paths (light grey thick arrows) are positioned on preferred rim *P–T* conditions and indicate the trajectory of the last *P–T* path segment calculated for overthrust terranes: Big Staurolite nappe, Central New England (I–II) and the North Cascade Range and Coast Mountains, US and Canadian Cordillera (III) metapelites. Roman numerals: I, Bellows Falls area (Spear *et al*., 2002); II, Mascoma–Orfordville area (Kohn *et al*., 1992); III, Nason terrane and Southern British Columbia area (Whitney *et al*., 1999). The calculated prograde segment of modelling *P–T* trajectory (grey thick arrows) using two-dimensional thermal–mechanical model during continental collision consistently show increases in pressure with little or no heating (IV, Jamieson *et al*., 2002; V, Huerta *et al*., 1999). The aluminosilicate phase diagram is reproduced from Holland & Powell (1985).

formed by using the MATHEMATICA5.0 computer software (Wolfram, 2003), and especially its built-in functions. The results are presented in Table 3. Calculated pressure estimates error values for several samples ranged from *c.* ± 0.28 to ± 0.46. This range correlates well with the most frequently cited uncertainties in the literature of ± 0.5 kbar for typical barometers (Kohn & Spear, 1991).

In order to evaluate the difference in calculated pressure values more precisely, statistical analysis of these estimates was carried out based on comparison of the mean values and standard deviations between adjacent zones using Student's *t* and Fisher's tests according to the methods described by Urbakh (1964). These data reveal that, at the 95% confidence level, all

four sets of pressure estimates demonstrate a significant difference in peak metamorphic pressures in metapelites of each metamorphic zone (Likhanov, 2003). This implies that various metamorphic zones differ in pressure conditions and do not overlap (taking into account the calculated errors in pressure estimates).

P–T path calculations

Spear & Selverstone (1983) developed a technique for estimating *P–T* paths from chemically zoned metamorphic minerals, so that the chemistry of garnet, mica, chlorite and plagioclase in critical mineral assemblages allow the evaluation of the *P–T* history of garnet-bearing rocks in zones II–IV. The method uses an analytical formulation of the phase equilibria of a given mineral assemblage in such a way that changes in the composition of coexisting minerals in the assemblage can be monitored as functions of changing *P* and *T*. It is assumed that the phases were in equilibrium during the entire period of mineral growth and zoning.

The computer program PTPATH by Spear (1986) was used in modelling *P–T* paths based on chemical zoning profiles in garnet, combined with mineral chemistry from the other minerals in the assemblages. For such calculations, it is necessary to specify the assemblage in which the garnet grew. The microtextural observations suggest that the last increment of garnet growth was with the assemblage garnet + staurolite + chlorite + biotite + muscovite + plagioclase + quartz. It is assumed that this assemblage (the current matrix assemblage) was present throughout garnet growth. In the zoning traverses analysed here, garnet is characterized by a slight increase of grossular component from core to rim, whereas plagioclase is commonly unzoned. Because of the low variance of this assemblage, no assumptions about plagioclase zoning were necessary as input parameters. The one exception is garnet and plagioclase from the more magnesian rocks of the inner zone which show a more abrupt increase in grossular component and anorthite component to sodic andesine from core to rim. It was assumed that the change in plagioclase (sample 34 of Zone IV) from core to rim (X_{An} = 0.420–0.334) can be correlated with the core-rim growth of the garnet, and that these compositional changes in plagioclase are dispersed smoothly over the zoning profile. This assumption is warranted as in a closed system, growth of garnet requires consumption of anorthite component and a shift of remaining plagioclase composition toward albite (Spear *et al*., 1990). This relationship is not substantially altered for most *P–T* paths if NaK_{-1} exchange in muscovite is accounted for (Spear *et al*., 1990). Temperature and pressure estimates for the begin of garnet growth have been obtained by the simultaneous consideration of garnet core plus matrix biotite thermometry (Kleemann & Reinhardt, 1994), which gives a mean value between the two

experimental calibrations of Ferry & Spear (1978) and Perchuk & Lavrent'eva (1983), with Grt–Bt–Ms–Pl barometry (Ghent & Stout (1981), with modifications by Hodges & Crowley (1985).

The calculated *P–T* paths, derived from garnet zoning patterns and garnet and plagioclase compositional correlations, are shown in Fig. 5. All *P–T* paths have nearly identical slopes, and differ mainly in the length of the recorded *P–T* growth history. In all cases the *P–T* trajectory documents increasing pressure (from 1.5 to 2.5 kbar) associated with only minor heating (up to 20 ± 15 °C), thus suggesting nearly isothermal loading (Thompson & England, 1984). The conclusion of substantial burial during garnet growth is consistent with the textural evidence for strong progressive compression, transposing the initial fabric into a second foliation during garnet growth. The *P–T* paths correlate well with both the petrographically observed mineral parageneses and with the *P–T* conditions estimated from thermobarometry and *P–T* evolution of metamorphic rocks from some collisional orogens in central New England (Kohn *et al*., 1992; Spear *et al*., 2002) and the North Cascade Range and Coast Mountains (Whitney *et al*., 1999) resulting from crustal thickening caused by thrusting (Fig. 5). The calculated *P–T* trajectories, inferred from two-dimensional thermal–mechanical modelling during continental collision in overthrust terranes, display *P–T* paths broadly similar to those presented here (Fig. 5).

Moreover, these results are consistent with metamorphic recrystallization having occurred during thrust emplacement of the tectonically overlying PUP. Detailed mass-transfer analysis of all mineral reactions, which form Ky–St–Ms–Qtz pseudomorphs and minerals in the adjacent matrix, were reported by Likhanov & Reverdatto (2002). The net mass balance obtained is in good agreement with reactions proposed by Whitney *et al*. (1995, 1996) for relatively aluminous, Fe-rich pelitic schists from Dutchess County (USA) and British Columbia (Canada), and with the *P–T* stability fields of the key assemblages predicted by the petrogenetic grid of Likhanov *et al*. (2004) for ferruginous–aluminous metapelites in the KFMASH system.

It was shown that the very large volume ($-\Delta V =$ 42–49%) and small entropy effects characterize the calculated reactions. It indicates that the prograde evolution of chemical and modal compositions of minerals during metamorphism was controlled by gradual pressure increase (at nearly constant temperature) accompanied by deformation within the bulk composition of the protolith. The calculated mineral reactions, inferred to have occurred during pressure increase in rocks overlapped by the Panimba thrust also confirm the possibility of prograde transformation of andalusite to kyanite.

A question that must be posed if such *P–T* paths are to be used for tectonic interpretation, is: how do errors propagate through the calculations? Spear & Rumble

(1986) presented the results of a Monte Carlo simulation on *P–T* paths computed by propagating microprobe errors using the Spear & Selverstone (1983) method. Calculated values of the pressure uncertainties for well-characterized samples are in the order of ±0.15 to ±0.5 kbar. It was also shown that the discrepancy between calculated *P–T* paths can all be largely attributed to the propagation of microprobe errors. Errors in the thermodynamic database will affect all parts in a similar fashion. Errors in activity models do not propagate into large errors in computed *P–T* paths as long as the extrapolation from the reference *P–T–X* conditions is not large. Therefore, *P–T* paths computed in this manner may be interpreted with a reasonable degree of confidence.

SUMMARY AND INTERPRETATION OF *P–T* EVOLUTION

The combined petrological and microtextural observations presented above provide constraints on the metamorphic history of metapelites in the Transangarian region of the Yenisey Ridge and show evidence of two superimposed metamorphic events. Based on the data derived in this study, it can be concluded that a middle Proterozoic (1100 ± 50 Ma), low-pressure metamorphic event produced andalusite-bearing assemblages in the KLP (3.5–4 kbar; 540–560 °C). In the late Proterozoic (850 ± 50 Ma), these rocks were subjected to nearly isothermal, progressive pressure increase and penetrative deformation in the vicinity of the Panimba overthrust (4.5–6.7 kbar; 540–600 °C), and were overprinted by medium-pressure, kyanite-bearing regional metamorphic mineral assemblages. The metapelites exhibit progressively higher peak pressures towards the presently exposed trace of the Paninmba thrust, concomitant with an increasingly intensive obliteration of the middle Proterozoic regional fabric and superposition of a new fabric system.

In the following sections the data and observations presented above are used to construct a tectono-thermal model describing the tectonic mechanism and temperature regime of the area studied with its nearly isothermal loading.

Tectonic mechanism

Several possible tectonic models have been proposed in literature to explain the pressure increase towards the thrust zone, whereby the most important sources of significant tectonic stress arise from isostatically compensated loads and from plate boundary forces:
(1) The initially horizontal or sub-horizontal low-pressure metamorphic rock sequences were folded and preserved either as a fold limb or as a monocline. So, in the eastern part of the structure, these rocks would represent either the core of a fold or the most deep-seated part of a monocline. However, geothermobarometry indicates a pressure difference of 1.5–2.5 kbar

over a horizontal distance of 7 km at nearly constant temperature. In this model, the temperature would also have to increase toward the thrust zone (i.e. from west to east) by at least 70–140 °C, if a thermal gradient of 10–20 °C km^{-1} is assumed (e.g. Ruppel & Hodges, 1994).

(2) The revealed increase in pressure in the vicinity of the thrust could have been a result of the separate movement of crustal slices which were sequentially pushed up from different depth levels during thrusting process (e.g. Beaumont *et al.*, 2001). However, this model of 'strike–slip structural pattern' lacks the support of geological evidence for the presence of tectonic contacts and high lateral temperature gradients between adjacent metamorphic zones.

(3) The pressure increase could be related to plate boundary forces such as ridge push (e.g. Kusznir & Park, 1984). Petrini & Podladchikov (2000) investigated the pressure distribution with depth in regions undergoing horizontal shortening and experiencing crustal thickening. Their two-dimensional modelling results show that, in compressive tectonic settings, the pressure values range from one to two times the lithostatic values. However, in most cases, the magnitude of nonhydrostatic corrections to pressure estimates is smaller than the uncertainty of geobarometers. Laboratory experiments on rheology of the rocks show that the average stress level at a depth of 15–20 km within a continental plate arising from such sources is likely to lie within the range 0.2–0.3 kbar, if distributed over the whole lithospheric plate at a geologically realistic strain rate of 10^{-17}–10^{-14} s^{-1} (Strehlau & Meissner, 1987). Such stress is not sufficient to achieve overpressures of as much as 1.5–2 kbar.

(4) The increase in lithostatic pressure could be because of loading by overlying magma (e.g. Brown & Walker, 1993). The magma loading model is based in part on the observation that pressures in metapelitic rocks decrease away from granitoid plutons. As noted above, however, comparable intermediate pressures are recorded in rocks irrespective of their proximity to plutons. Furthermore, magmatism plays a particularly sensitive role in models of crustal thickening, because of the higher heat content of magma in comparison

with the base of a thrust sheet, and the significant thermal contribution of the heat of crystallization of magma (typical values for latent heat are orders of magnitude larger than heat production because of radioactive decay). In addition, depending on intrusion rates and volume, advective heating by magmatism is one to several orders of magnitude faster than advective heating by thrusting [e.g. compare rates in Ruppel & Hodges (1994) to Paterson & Tobisch (1992)].

As these models are inconsistent with petrological evidence, it remains to be discussed whether the observed *P–T* paths are consistent with a model of thrust emplacement (England & Thompson, 1984), and, if so, what they reveal about the tectonic evolution of the study region. All *P–T* paths observed suggest nearly isothermal loading, in accordance with the emplacement of a thrust sheet, such that the change in pressure corresponds to a change in depth of a given sample. Our preferred model for the tectonic evolution of the rocks is presented in Fig. 6, in an attempt to integrate the results of this study into a coherent model. Prior to thrusting, the pressures recorded in the low-pressure, andalusite-bearing rocks suggest a depth of *c.* 15–17 km. During thrusting, these rocks experienced a pressure increase of 1.5–2 kbar, equivalent to an increase in burial depths of 5–7 km. The post-thrusting pressures (4.5–6.7 kbar) imply the depth of rocks was on the order of *c.* 20–24 km, which is a measure of the total tectonic overburden. This could be explained by tectonic crustal thickening because of the southwestward thrusting of the PUP onto the KLP. In addition, it is clear that *c.* 15 km of the upper part of the KLP directly beneath the overthrust must have been tectonically removed in order to juxtapose at the present erosion surface, as presently observed, Zone IV rocks with the Panimba thrust (Fig. 6).

Thermal model

The main difficulty in such a model is the isothermal nature of the loading process. One of the possible mechanisms discussed in the literature is subduction/ thrusting followed by fast uplift. In this model, the subducted/underthrust slab fails to equilibrate
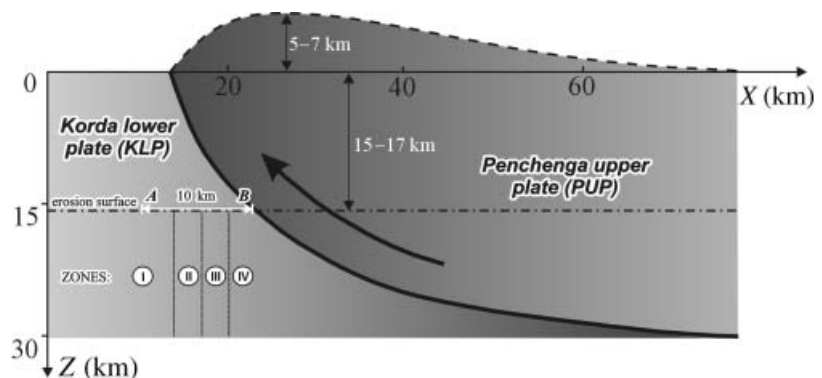
Fig. 6. Schematic tectonic model to explain the evolution of the metamorphic zones in the study area in terms of crustal thickening because of the north-eastward-dipping Panimba thrust (heavy line), along which metacarbonates of the PUP are thrust over metapelites of the KLP (arrow). Mantle heat flow is assumed to remain constant. White line A–B corresponds to position of cross-section A–B through the KLP metapelites in Fig. 1d.

thermally before the rocks are brought back near the surface. Thermal–mechanical modelling provides constraints on the likely mechanism of loading because *P*–*T* paths inferred from thermobarometric result can be compared with paths predicted by models calculated from heat transfer equations for crustal thickening. Early models for the thermal effects of thrust emplacement in the vicinity of major thrust zones (e.g. England & Thompson, 1984) relied on assumptions of instantaneous thrust emplacement and one-dimensional heat conduction. Later two-dimensional modelling of Ruppel & Hodges (1994) incorporated the effects of radiogenic heat and isostasy, and these authors examined the effects of transient thrusting with variable thrust rates, thrust dips and exhumation rates on *P*–*T* paths. Jamieson *et al.* (1998) used thermal models to examine the effects of tectonic redistribution of crust rich in heat-producing elements on the thermal and deformational history of small convergent orogens. Beaumont *et al.* (2001) and Jamieson *et al.* (2002) investigated the thermal and mechanical evolution, and resulting metamorphic response, of large convergent orogens that are driven by subduction of lithosphere. Most of the burial *P*–*T* paths produced by these models are very steep (Fig. 5), a style observed in many overthrust terranes. Shi & Wang (1987); Karabinos & Ketchman (1988) and Spear *et al.* (1989) have presented two-dimensional thermal models of thrusting that demonstrate that rocks of the lower plate of a thrust system cannot undergo isothermal loading during thrusting unless the rate of thrusting is unreasonably fast (for example, on the order of metres per year). Spear *et al.* (1989) did demonstrate, however, that isothermal loading could occur in the middle plate of a multi-plate system if both bounding thrusts move simultaneously. In such a middle plate, heating from above is balanced by cooling from below, so that the temperature remains relatively constant. For this model to apply to the Transangarian region, however, would require that the rocks beneath the KLP be allochthonous and underlain by another thrust, in contradiction to the geological situation in the study area.

On the other hand, it would be possible to avoid this problem, having assumed, that during the substantial time break between the middle and late Proterozoic events, the low-pressure metamorphic rock sequences experienced a period of cooling during uplift and erosion, which was followed by subsequent heating during the late Proterozoic tectonic loading, as predicted by the thermal models of England & Thompson (1984). As discussed previously, no unequivocal geological evidence of cooling in this region has been presented. Mineralogical and microtextural features, such as partial pseudomorphs and veining, leaving optically continuous relics from an earlier assemblage, and distinctly expressed zoned reaction microtextures (indicating simultaneous growth of new minerals after

upper grade minerals), used to infer retrograde effects are largely absent in these rocks. Near-rim compositions of all ferromagnesian mineral phases also show no evidence for retrograde cation exchange processes. These data are consistent with a stratigraphical sequence of sedimentary rocks of middle to late Proterozoic age, which were formed as a result of consecutive accumulation of deep-water sediments under subsidence of the basin floor of the Palaeoasian ocean.

The two-dimensional nature of above mentioned models requires that not only the vertical extent, but also the horizontal tectonic motion, of thrust faulting lie within physically realistic limits (Ruppel & Hodges, 1994). The application of such models for this region is limited by the lack of the necessary input parameters, such as thrusting and erosion rates, and thrust geometry. Therefore, we propose an alternative interpretation of the observed tectono-metamorphic evolution of the study area. The simplified model used here makes no attempt at reproducing these effects of horizontal fault geometry as in real settings thrust faults do not have constant dip and often propagate stepwise. Unlike some previous models of continental crustal thickened by thrusting (Peacock, 1989; Huerta *et al.*, 1998), we suggest that the two plates (KLP & PUP) on both sides of the thrust have different thermal conductivities and heat generation properties, in order to account for the lack of significant heating of the underthrusted rocks. Previous models imply that, after fast underthrusting of slabs with similar steady-state geotherms, the lower-plate rocks should be heated by 150 °C (Ruppel & Hodges, 1994). However, the significant difference in the rock types on both sides of the Panimba thrust suggests that differences in radioactive heat sources, thermal conductivity coefficients and, therefore, steady-state geotherms must be accounted for.

In order to demonstrate the existence of an overthrusting mechanism, the problem of conductive heating when moving the hanging wall (PUP) relative to the footwall (KLP) along the steeply dipping thrust fault needs to be examined (Fig. 6). The one-dimensional lateral heating model is used to evaluate the temperature distribution along the horizontal sections A–B. Holding the overthrusting velocity constant along the fault leads to temperature increasing at point B, which depends on temperature gradient and exhumation rate in the upper plate. Prediction of the uplift velocity under which nearly isothermal loading condition is obeyed would be useful.

The temperature evolution is described by the one-dimensional heat transfer equation in the horizontal direction:

$$\frac{\mathrm{d}T}{\mathrm{d}t} = \kappa \frac{\partial^2 T}{\partial x^2}, \qquad (1)$$

where *t* is the time, *T* is the temperature and κ is the thermal diffusivity.

Boundary conditions of net horizontal heat flow at the right boundary (point B) and linearly increasing

temperature in time at the left boundary (point A) were imposed:

$$T(0, t) = T_0 + V\frac{\partial T}{\partial z}t, \qquad (2)$$

where z is the depth and V is the uplift velocity.

Initial condition is uniform temperature $T_0 = 500\ °C$ at the depth of 15 km (the present erosion surface):

$$T(x, 0) = T_0. \qquad (3)$$

In dimensionless form, the solution of equation (1) with boundary (2) and initial condition (3) may be expressed as (Carslaw & Jager, 1959):

$$\theta = \left\{1 + \text{erf}\left(\frac{x'}{2\sqrt{\tau}}\right)\right\} + \text{Pe}a\tau\left\{\left(1 + \frac{x'^2}{2\tau}\right)\text{erf}^*\left(\frac{x'}{2\sqrt{\tau}}\right)\right.$$
$$\left. - \frac{x'}{\sqrt{\pi\tau}}\exp\left(-\frac{x'^2}{4\tau}\right)\right\}, \qquad (4)$$

where $\text{Pe} = VL/\kappa$ is the Peclet number, L is the characteristic length scale, $a = \partial T/\partial z\sin\alpha$ is the reduced dimensionless geothermal gradient, α is the dip angle of fault at point B, τ is the dimensionless time, $x' = x/L$, $\theta = T/T_0$, $t = L^2/\kappa\tau$, $\text{erf}^*(x) = 1 - \text{erf}(x)$ is the complementary error function.

Figure 7 shows that an increasing temperature on the fault surface results in footwall heating being dependent on uplift velocity, which is expressed by Pe. As maximum temperature changes during metamorphism were small, and increased toward the thrust on average by 30 °C, the dimensionless thrust velocity corresponds
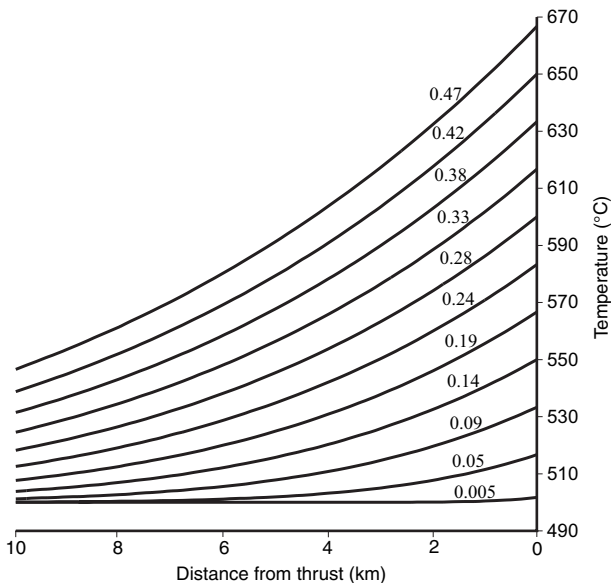
Fig. 7. Calculated temperature distribution as a function of Peclet number (dimensionless velocity of overthrusting) under condition of temperature increase on the right boundary. Initial temperature is taken to be as high as 500 °C. Numbers near curves correspond to Peclet number. Location of horizontal section A–B is shown in Fig. 6.

to $\text{Pe} = 0.09$. Knowing the Peclet number means it is possible to estimate the overthrusting velocity by using the total width of metamorphic zones of 10 km for the characteristic length scale L, 500 °C for the temperature value, reduced dimensionless geothermal gradient of 0.7 c. sin 45 ° for a, and $10^{-6}\ m^2\ s^{-1}$ for thermal diffusivity κ. Under these conditions, the thrust velocity must be less than $V \leqslant \text{Pe}\ \kappa/L = 0.09 \times 10^{-10}\ (m\ s^{-1}) \approx 300\ m\ Myr^{-1}$. This value is less than independently constrained estimates of uplifting and accretion rates in the orogenic collision events. For example, within the Himalayan thrust belt the rates of erosion and accretion derived from the evolution of metamorphic parameters, apatite fission-track data and $^{40}Ar/^{39}Ar$ analysis of detrital K-feldspar and muscovite, range from 0.5 to $1.8 \pm 0.7\ km\ Myr^{-1}$ (Copeland & Harrison, 1990; Hubbard et al., 1991; Huerta et al., 1999). The exhumation of ultrahigh pressure metamorphic rocks related to continent–continent collision occurred at the rate of over 13 km Myr^{-1} (Coleman & Wang, 1995). The thrusting velocity determined here of c. 300 m Myr^{-1} compares well with that obtained using P–T–t path reconstruction and numerical models in the overthrust terranes (England & Thompson, 1984; Peacock, 1989; Spear et al., 1991).

In order to estimate the possible temperature increase in the lower plate, the thermal evolution of two juxtaposed plates with different radioactive heat sources and thermal conductivities was considered. It is assumed that the evolution of the geotherm is controlled by the initial distribution of radioactive heat-generating elements in the overthrust and underthrust plates and by the heat conduction through the crust from the mantle. The instantaneous juxtaposition of a hot thrust nappe on a cold footwall leads to initiation of the 'sawtooth' geotherm and progressive heating of lower plate (Spear, 1993).

Analytical and numerical solutions to the differential equations concerning thermal conduction with radiogenic heat production have been used to substantiate the thrust model. One-dimensional, conductive heat transfer equation in a horizontal infinite plate H km thick can be represented by:

$$\frac{dT}{dt} = \frac{\lambda}{\rho C_p}\frac{\partial^2 T}{\partial z^2} + \frac{A}{\rho C_p}, \qquad (5)$$

where t (s) is time, T (°C) temperature, k (W m^{-1} K^{-1}) thermal conductivity, z (m) depth, ρ (kg m^{-3}) density, C_p (kJ kg^{-1}) isobaric specific heat and A (W m^{-3}) represents radiogenic heat sources.

It is appropriate to assume that the heat production because of radioactive elements decreases exponentially with depth (Turcotte & Shubert, 1982):

$$A = A_0\exp\left(\frac{-z}{D_r}\right). \qquad (6)$$

The upper boundary is maintained at $T_{\text{surf}} = 0\ °C$, and the lower boundary condition is a specified basal

heat flux, $Q = 30$ mW m^{-2}. Integration of Eq. (5) with appropriate boundary conditions gives the steady-state geotherm (Spear, 1993):

$$T = T_{\mathrm{surf}} + \frac{Qz}{\lambda} + \frac{A_0 D_{\mathrm{r}}^2}{\lambda}\left(1 - \mathrm{e}^{-z/D_{\mathrm{r}}}\right), \qquad (7)$$

where A_0 is the surface radiogenic heat production and $D_r = 10^4$ m is the depth constant.

As indicated above, the average thermal gradient in the rocks during peak metamorphism is lower than the gradients in many Precambrian terranes. However, there is an increasing awareness that the distribution of radiogenic heat production can influence the thermal structure of the crust (e.g. Huerta *et al.*, 1998). Using the concentrations of heat-producing elements in the KLP and PUP rocks (Table 4), heat generation in these rocks can be calculated on the basis of the Ljubimova (1968) model. In the case of five KLP metapelites the value averages 2.04 μW m^{-3} and for the PUP metacarbonates it is one order of magnitude lower, with $A_0 = 0.375$ μW m^{-3} (Table 4). The calculated geotherms for the PUP and KLP before and after thrusting are shown in Fig. 8. The curves in Fig. 8a are steady-state geotherms for a model crust with maximum values for the observed range of radioactive heat sources in the KLP and PUP. Thermal conductivities of metapelites and metacarbonates are assumed to be 1.5 and 2.5 W m^{-1} K, respectively, based on literature data for thermal conductivities of limestone and shale (Clark, 1966). The thrusting resulted in the KLP rocks being buried to depths of 20–24 km, as shown in Fig. 8b by the relative positions of the grey rectangles. The re-equilibrated steady-state geotherms after instantaneous thrusting of the 5–7 km-thick PUP are shown in Fig. 8b. These curves show a range of temperatures from a minimum range (curve 4) to maximum heat production (curve 3) for KLP and PUP rocks. The modelled results show that heat production in the KLP is the most important parameter. The steady-

Table 4. Concentrations of heat-producing elements and heat production (A_0) in KLP and PUP rocks.

	U	Th	K	A_0 (W kg^{-1})	A_0 (W m^{-3})
KLP metapelites					
51	2.0	16.1	2.70	7.2×10^{-10}	1.93×10^{-6}
59	2.1	14.7	2.42	6.8×10^{-10}	1.83×10^{-6}
63	2.4	14.7	2.00	6.9×10^{-10}	1.86×10^{-6}
34	3.1	17.0	1.65	8.1×10^{-10}	2.17×10^{-6}
74	3.3	18.6	2.08	8.8×10^{-10}	2.38×10^{-6}
Mean H					2.03×10^{-6}
PUP metacarbonates					
1	1.4	0.8	0.3	1.6×10^{-10}	4.39×10^{-7}
2	0.4	2.1	0.6	1.2×10^{-10}	3.11×10^{-7}
Mean H					3.75×10^{-7}

U and Th abundances in parts per million (determined by gamma-spectrometric analysis), K abundances in wt% (determined by gamma-spectrometric analysis).
In the table, 1 represents averaged U, Th and K contents, based on 32 analysis, from Zlobin *et al.* (1975) and 2 represents averaged U, Th and K contents, based on 16 analyses, from Nozhkin *et al.* (1975).
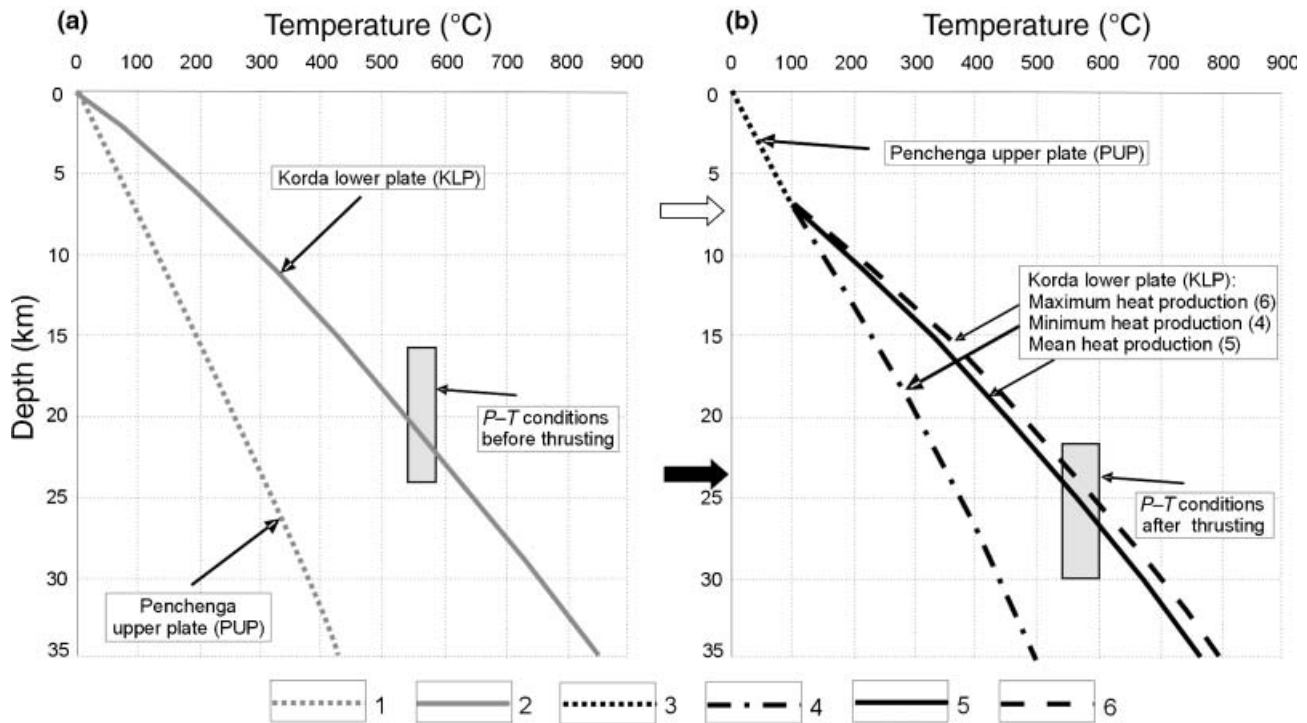
state geotherm (curve 5) constructed using the mean values of heat production for PUP and KLP rocks also passes through the *P–T* estimates of the medium-pressure rocks of zones II–IV in the vicinity of the thrust (Table 3). It is evident from Fig. 8 that there is only a small temperature increase when comparing the position of the maximum steady-state geotherms (curves 1 and 3) relative to the grey rectangle. This small increase is in a good agreement with the *P–T* paths shown in Fig. 5, and lends support to the validity of the proposed model.

The transient one-dimensional heat conduction in two-layered crust can be simulated using the finite difference method. Time integration of the heat flow equation was carried out using a second order accurate implicit Crank–Nicolson scheme. Figure 9 shows the calculated geotherms at four different stages of evolution and the equilibrium steady-state geotherm in the case of no erosion. It is assumed that the proportions and distribution of radioactive heat sources remain unchanged during thrusting in both of the plates and are described by Eq. (6), and the boundary conditions are the same. The maximum temperature increase in the KLP metapelites is only observed near the interface boundary between plates (Fig. 9). After thrusting, the lower plate is significantly heated up to 90 °C in the depth range from 7 to 20 km. Below this depth the difference between initial and final, steady-state temperature at a depth of over 20 km is < 10 °C. Such a small increase is because of low radioactive heat generation in the PUP as compared with the KLP. In the case of erosion of the upper plate, an increase in temperature will be smaller because of heat removal because of plate thickness decreasing.

CONCLUSIONS

In summary, the sequence of events envisaged is as follows. An early middle Proterozoic event produced low-pressure, andalusite-bearing assemblages (3.5–4 kbar; 540–560 °C). These rocks are represented as D1 and interpreted as having formed before thrusting. During a subsequent late Proterozoic event, these rocks underwent a nearly isothermal gradual pressure increase (4.5–6.7 kbar; 540–600 °C) because of south-west directed thrusting of the PUP metacarbonates onto the KLP metapelites, giving rise to D2 deformation, as a result of which low-pressure metamorphic effects were overprinted by medium-pressure regional metamorphic mineral assemblages and textures. As Fig. 5 illustrates, this pressure increase was sufficient to shift all low-pressure rocks in the over-thrust terrane into the kyanite *P–T* stability field. Thermo-physical computational results show that only a small temperature increase of the rocks beneath the thrust plane took place, because the juxtaposed rocks differ significantly in their thermo-physical and heat-producing properties. The proposed model for tectono-metamorphic evolution of the study area,

Fig. 8. Calculated steady-state geotherms for the PUP (2) and KLP rocks (1, 3, 4 and 5) before (a) and after (b) thrusting. The grey rectangle indicates the depth–temperature coordinates determined for the medium-pressure rocks of the II–IV zones. White arrow shows PUP/KLP boundary, grey arrow indicates assumed present erosion surface. Thermal conductivities 1.5 W m^{-1} K in KLP rocks and 2.5 W m^{-1} K in PUP rocks were used to calculate steady-state geotherms (1–5). The following heat production parameters were used: 2.38 μW m^{-3} in KLP rocks and 0.375 μW m^{-3} in PUP rocks (for curves 2 & 1); 2.38 μW m^{-3} in KLP rocks and 0.439 μW m^{-3} in PUP rocks (for curve 3); 1.86 μW m^{-3} in KLP rocks and 0.311 μW m^{-3} in PUP rocks (for curve 4); and 2.03 μW m^{-3} in KLP rocks and 0.375 μW m^{-3} PUP rocks (for curve 5). Other input parameters are reported in the text.
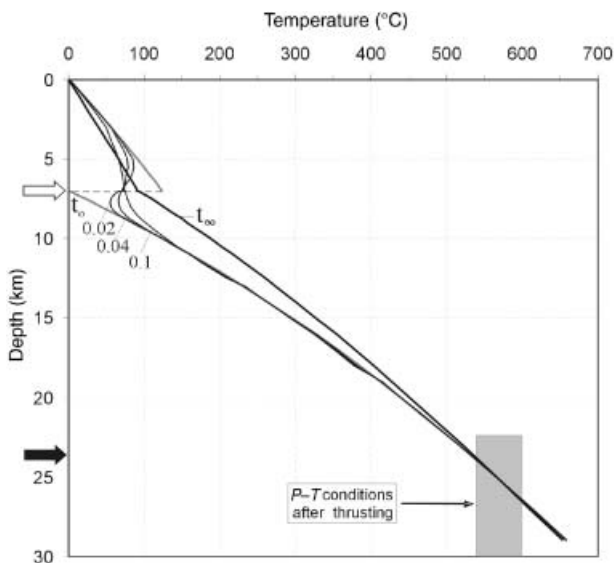
Fig. 9. Temperature–depth plot showing thermal evolution of thickened crust in the overthrust model. Curve labelled t_0 represents initial (sawtooth) geotherm characteristic of instantaneous overthrusting. Curves labelled with time in million of years after thrusting. Curve labelled t_∞ represents steady-state geotherm approached after tens of million of years. Other symbols are the same as in Fig. 8.

calculated within a framework of crustal thickening by southwestward thrusting, explains a number of features (e.g. the origin of kyanite after andalusite, common increase in garnet grossular content from core to rim, the gradual change in recorded pressure between low- and medium-pressure rocks, small temperature increase, etc.) associated with this tectonic phenomenon and confirms the possibility of nearly isothermal loading during overthrusting.

The interpretation of the observed tectono-metamorphic evolution of the study area offered in this paper is broadly consistent with all the geological features and petrological evidence. The coupled thermal-mechanical model presented here corresponds well with P–T paths inferred from thermobarometric results from this study. Furthermore, the coupled thermal-mechanical model correlates with P–T trajectories predicted by two-dimensional thermal models calculated for different crustal thickening and exhumation histories (e.g. Beaumont *et al.*, 2001; Jamieson *et al.*, 2002). Although less sophisticated than two-dimensional models, a one-dimensional thermal model of nearly isothermal loading during overthrusting serves as a useful step in evaluating the relation between observed P–T paths and tectonic mechanisms

of thrust loading. Testing of this model can best be achieved from detailed analysis of the timing of peak metamorphism across thrust fault from petrologically well-characterized structural levels that enable the determination of the real thrust rates.

ACKNOWLEDGEMENTS

REFERENCES

Ague, J. J., 1991. Evidence for major mass transfer and volume strain during regional metamorphism of pelites. *Geology*, **19**, 855–858.

Baker, A. J., 1987. Models for the tectonothermal evolution of the eastern Dalradian of Scotland. *Journal of Metamorphic Geology*, **5**, 101–118.

Beaumont, C., Jamieson, R. A., Nguyen, M. H. & Lee, B., 2001. Himalayan tectonics explained by extrusion of a low-viscosity crustal channel coupled to focused surface denudation. *Nature*, **414**, 738–742.

Beddoe-Stephens, B., 1990. Pressures and temperatures of Dalradian metamorphism and the andalusite–kyanite transformation in the northeast Grampians. *Scottish Journal of Geology*, **26**, 3–14.

Brown, E. H., 1996. High-pressure metamorphism caused by magma loading in Fiordland, New Zealand. *Journal of Metamorphic Geology*, **14**, 441–452.

Brown, E. H. & Walker, N. W., 1993. A magma-loading model for Barrovian metamorphism in the Southeast Coast Plutonic Complex, British Columbia and Washington. *Geological Society of America Bulletin*, **105**, 479–500.

Bucher-Nurminen, K., 1987. A recalibration of the chlorite–biotite–muscovite geobarometer. *Contribution to Mineralogy and Petrology*, **96**, 519–522.

Carslaw, H. S. & Jager, E., 1959. *Conduction of Heat in Solids*, 2nd edn. Clarendon Press, Oxford, UK.

Clark, C. P., 1966. *Handbook of Physical Constants*. Geological Society of America Memoir 97, Yale University, New Haven, CT, USA.

Clarke, G. L., Guirard, M., Powell, R. & Burg, J. R., 1987. Metamorphism in the Olary Block, South Australia: compression with cooling in a Proterozoic fold belt. *Journal of Metamorphic Geology*, **5**, 291–306.

Coleman, R. G. & Wang, X., 1995. Overview of geology and tectonics of UHPM. In: *Ultrahigh Pressure Metamorphism* (eds Coleman, R. G. & Wang, X.), pp. 1–32. University Press, Cambridge, UK.

Copeland, P. & Harrison, T. M., 1990. Episodic rapid uplift in the Himalaya revealed by $^{40}Ar/^{39}Ar$ analysis of detrital K-feldspar and muscovite, Bengal fan. *Geology*, **10**, 354–357.

Crawford, M. L. & Mark, L. E., 1982. Evidence from metamorphic rocks for overthrusting. Pennsylvania Piedmont, USA. *Canadian Mineralogist*, **20**, 333–347.

Dazenko, V. M., 1984. *Granitoid Magmatism of the South-West Edge of the Siberian Platform*. Nauka Press, Novosibirsk (in Russian).

Dempster, T. J., 1985. Uplift patterns and orogenic evolution in the Scottish Dalradian. *Journal of Geological Society of London*, **142**, 111–128.

Droop, G. T. R., 1985. Alpine metamorphism in the south-east Tauern Window, Austria: 1. *P–T* variations in space and time. *Journal of Metamorphic Geology*, **3**, 371–402.

England, P. C. & Richardson, S. W., 1977. The influence of erosion upon the mineral facies of rocks from different metamorphic environments. *Journal of Geological Society of London*, **134**, 201–213.

England, P. C. & Thompson, A. B., 1984. Pressure–temperature paths of regional metamorphism. I. Heat transfer during the evolution of regions of thickened continental crust. *Journal of Petrology*, **25**, 894–928.

Essene, E. J., 1989. The current status of thermobarometry in metamorphic rocks. In: *Evolution of Metamorphic Belts, Special Publication, 43* (eds Daly, J. S., Cliff, R. A. & Yardley, B. W. D.), pp. 1–44. Geological Society, London.

Ferry, J. M. & Spear, F. S., 1978. Experimental calibration of the partitioning of Fe and Mg between biotite and garnet. *Contributions to Mineralogy and Petrology*, **66**, 113–117.

Ghent, E. D. & Stout, M. Z., 1981. Geobarometry and geothermometry of plagioclase–biotite–garnet–muscovite assemblages. *Contributions to Mineralogy and Petrology*, **76**, 92–97.

Giorgetti, G., Memmi, I., Likhanov, I. I. & Reverdatto, V. V., 2001. TEM study of textural relationships between staurolite and quartz in polymetamorphic Al-rich schists from Transangarian region (Yenisei Ridge, Russia). In: *Proceedings International Conference on Crystallogenesis and Mineralogy* (ed. Bulakh, A. G.), pp. 120–121, Russian Mineralogical Society, St Petersburg, Russia.

Grambling, J. A., 1986. A regional gradient in the composition of metamorphic fluids in pelitic schists, Pecos Baldy, New Mexico. *Contributions to Mineralogy and Petrology*, **94**, 149–164.

Hodges, K. V. & Crowley, P. D., 1985. Error estimation and empirical geothermobarometry for pelitic system. *American Mineralogist*, **70**, 702–709.

Hodges, K. V. & McKenna, L. W., 1987. Realistic propagation of uncertainties in geologic thermobarometry. *American Mineralogist*, **72**, 671–680.

Hodges, K. V. & Spear, F. S., 1982. Geothermometry, geobarometry and the Al_2SiO_5 triple point at Mt. Moosilauke, New Hampshire. *American Mineralogist*, **67**, 1118–1134.

Hoisch, T. D., 1989. A muscovite–biotite geothermometer. *American Mineralogist*, **74**, 565–572.

Hoisch, T. D., 1990. Empirical calibration of six geobarometers for the mineral assemblage quartz + muscovite + biotite + plagioclase + garnet. *Contributions to Mineralogy and Petrology*, **104**, 225–234.

Hoisch, T. D., 1991. Equilibria within the mineral assemblage quartz + muscovite + biotite + garnet + plagioclase and implications for the mixing properties of octahedrally coordinated cations in muscovite and biotite. *Contributions to Mineralogy and Petrology*, **108**, 43–54.

Holdaway, M. J., Dutrow, B. L. & Hinton, R. W., 1988. Devonian and Carboniferous metamorphism in west-central Maine: the muscovite–almandine geobarometer and the staurolite problem revisited. *American Mineralogist*, **73**, 20–47.

Holdaway, M. J., Mukhopadhyay, B., Dyar, M. D., Guidotti, C. V. & Dutrow, B. L., 1997. Garnet–biotite geothermometry revised: New Margules parameters and a natural specimen data set from Maine. *American Mineralogist*, **82**, 582–595.

Holland, T. J. B. & Powell, R., 1985. An internally consistent thermodynamic dataset with uncertainties and correlations: 2. Data and results. *Journal of Metamorphic Geology*, **3**, 343–370.

Holland, T. J. B. & Powell, R., 1990. An enlarged and updated internally consistent thermodynamic dataset with uncertainties and correlations: the system K_2O–Na_2O–CaO–MgO–FeO–Fe_2O_3–Al_2O_3–TiO_2–SiO_2–C–H_2–O_2. *Journal of Metamorphic Geology*, **6**, 89–124.

Holland, T. J. B. & Powell, R., 1998. An internally consistent thermodynamic data set for phases of petrological interest. *Journal of Metamorphic Geology*, **16**, 309–343.

Hollister, L. S., 1969. Metastable paragenetic sequence of andalusite, kyanite, and sillimanite, Kwoeik area, British Columbia. *American Journal of Sciences*, **267**, 352–370.

Hubbard, M., Royden, L., Hodges, K., 1991. Constraints on unroofing rates in the High Himalaya, eastern Nepal. *Tectonics*, **10**, 287–298.

Huerta, A. D., Royden, L. H. & Hodges, K. V., 1998. The thermal structure of collisional orogens as a response to accretion, erosion, and radiogenic heating. *Journal of Geophysical Research*, **103**, 15287–15302.

Huerta, A. D., Royden, L. H. & Hodges, K. V., 1999. The effects of accretion, erosion and radiogenic heat on the metamorphic evolution of collisional orogens. *Journal of Metamorphic Geology*, **17**, 349–366.

Jamieson, R. A., Beaumont, C., Fullsack, P. & Lee, B., 1998. Barrovian regional metamorphism: Where's the heat? In: *What Drives Metamorphism and Metamorphic Reactions? Special Publication, 138* (eds Treloar, P. J. & O'Brien, P. J.), pp. 23–45. Geological Society, London.

Jamieson, R. A., Beaumont, C., Nguyen, M. H. & Lee, B., 2002. Interaction of metamorphism, deformation and exhumation in large convergent orogens. *Journal of Metamorphic Geology*, **20**, 9–24.

Karabinos, P. & Ketchman, R., 1988. Thermal structure of active thrust belts. *Journal of Metamorphic Geology*, **6**, 559–570.

Kerrick, D. M., 1990. *The Al_2SiO_5 Polymorphs.* Mineralogical Society of America, Washington, DC.

Khabarov, E. M., 1994. Formations and evolution of the Riphean sedimentation of the eastern zones of the Yenisey Ridge. *Russian Geology and Geophysics*, **35**, 34–42.

Kleemann, U. & Reinhardt, J., 1994. Garnet–biotite thermometry revisited: the effect of Al^{VI} and Ti in biotite. *European Journal of Mineralogy*, **6**, 925–941.

Kohn, M. J. & Spear, F. S., 1991. Error propagation for barometers. *American Mineralogist*, **76**, 138–147.

Kohn, M. J., Orange, D. L., Spear, F. S., Rumble, D., III, Harrison, T. M., 1992. Pressure, temperature, and structural evolution of west-central New Hampshire: hot thrusts over cold basement. *Journal of Petrology*, **33**, 521–556.

Kornev, T. Y., 1986. *Evolution of Magmatism and Mineralization in Time.* Nedra Press, Moscow (in Russian).

Kozlov, P. S., 1994. *Petrology, petrochemistry, and metamorphism of rocks in the Transangararian region of the Yenisey Ridge.* PhD Thesis, Novosibirsk University Press, Russia (in Russian).

Kretz, R., 1983. Symbols for rock-forming minerals. *American Mineralogist*, **68**, 277–279.

Kusznir, N. J. & Park, R. G., 1984. The strength of intraplate lithosphere. *Physics of the Earth and Planetary Interiors*, **36**, 224–235.

Likhanov, I. I., 2003. *Mineral reactions and mass-transfer during low- and medium-pressure metamorphism.* Doctor of Sciences Thesis, Geo Press, Novosibirsk (in Russian).

Likhanov, I. I., & Reverdatto, V. V., 2002. Mass transfer during andalusite replacement by kyanite in Al- and Fe-rich metapelites in the Yenisei Range. *Petrology*, **10**, 541–558.

Likhanov, I. I., Sheplev, V. S., Reverdatto, V. V. & Kozlov, P. S., 1998. Contact metamorphism of ferriginous metapelites at high pressure in the Trans Angara region, Yenisey Range. *Transactions (Doklady) of the Russian Academy of Sciences*, **363**, 1107–1110.

Likhanov, I. I., Sheplev, V. S., Reverdatto, V. V., Kozlov, P. S. & Kireev, A. D., 1999. The isochemical nature of the contact metamorphism of high-alumina metapelites in the Ayakhta granitoid massif, Yenisey Range. *Russian Geology and Geophysics*, **40**, 91–98.

Likhanov, I. I., Polyansky, O. P., Kozlov, P. S., *et al.*, 2000. Replacement of andalusite by kyanite with increasing pressure at a low geothermal gradient in metapelites of the Yenisey Ridge. *Transactions (Doklady) of the Russian Academy of Sciences*, **375**, 1411–1415.

Likhanov, I. I., Reverdatto, V. V., Sheplev, V. S., Verschinin, A. E. & Kozlov, P. S., 2001. Contact metamorphism of Fe- and Al-rich metapelites in the Transangarian region of the Yenisei Ridge, eastern Siberia, Russia. *Lithos*, **58**, 55–80.

Likhanov, I. I., Reverdatto, V. V. & Selyatitskii, A. Y., 2004. Petrogenetic grid for ferruginous-aluminous metapelites in the K_2O–FeO–MgO–Al_2O_3–SiO_2–H_2O. *Transactions (Doklady) of the Russian Academy of Sciences*, **394**, 46–49.

Ljubimova, E. A., 1968. *Thermics of Earth and Moon.* Nauka, Moscow (in Russian).

Loosveld, R. J. H., Etheridge, M. A., 1990. A model for low-pressure facies metamorphism during crustal thickening. *Journal of Metamorphic Geology*, **8**, 257–267.

Nozhkin, A. D., Krendelev, F. P. & Myronov, A. G., 1975. Radioactive elements in Precambrian of Yenisey Range. In: *Radioactive Elements in Rocks* (ed. Kuznetsov, V. A.), pp. 183–189. Nauka, Novosibirsk (in Russian).

Passchier, C. W. & Trouw, R. A. J., 1996. *Microtectonics.* Springer-Verlag, Berlin.

Paterson, S. R. & Tobisch, O. T., 1992. Rates and progress in magmatic arcs- implications for the timing and nature of pluton emplacement and wall rock deformation. *Journal of Structural Geology*, **14**, 291–300.

Peacock, S. M., 1989. Numerical constraints on rates of metamorphism, fluid production, and fluid flux during regional metamorphism. *Geological Society of America Bulletin*, **101**, 476–485.

Perchuk, L. L., 1991. Derivation of a thermodynamically consistent set of geothermometers and geobarometers for metamorphic and magmatic rocks. In: *Progress in Metamorphic and Magmatic Petrology* (ed. Perchuk, L. L.), pp. 93–112. Cambridge University Press, Cambridge, UK.

Perchuk, L. L. & Lavrent'eva, I. V., 1983. Experimental investigation of exchange equilibria in the system cordierite-garnet-biotite. In: *Kinetics and Equilibrium in Mineral Reactions* (ed. Saxena, S. K.), pp. 199–239. Springer, Berlin.

Petrini, K. & Podladchikov, Yu., 2000. Lithospheric pressure–depth relationship in compressive regions of thickened crust. *Journal of Metamorphic Geology*, **18**, 67–77.

Postel'nikov, E. S., 1990. Upper Proterozoic structures and formations of the eastern slope of the Yenisey Ridge. *Bulletin of Moscow Society of Nature Investigators*, **65**, 14–31 (in Russian).

Powell, R. & Evans, J. A., 1983. A new geobarometer for the assemblage biotite–muscovite–chlorite–quartz. *Journal of Metamorphic Geology*, **1**, 331–336.

Powell, R. & Holland, T. J. B., 1988. An internally consistent thermodynamic dataset with uncertainties and correlations: 3. Application to geobarometry, worked examples and a computer program. *Journal of Metamorphic Geology*, **6**, 173–204.

Powell, R. & Holland, T. J. B., 1994. Optimal geothermometry and geobarometry. *American Mineralogist*, **79**, 120–133.

Ruppel, C. & Hodges, K. V., 1994. Pressure–temperature–time paths from two-dimensional thermal models: prograde, retrograde and inverted metamorphism. *Tectonics*, **13**, 17–44.

Shaw, D. M., 1956. Geochemistry of pelitic rocks. Part III: Major elements and general geochemistry. *Geological Society of America Bulletin*, **67**, 913–934.

Shi, Y. & Wang, C., 1987. Two-dimensional modeling of the *P–T* paths of regional metamorphism in simple overthrust terranes. *Geology*, **15**, 1048–1051.

Spear, F. S., 1986. PTPATH: a FORTRAN program to calculate pressure–temperature paths from zoned metamorphic garnets. *Computers and Geosciences*, **12**, 247–266.

Spear, F. S., 1989. Relative thermobarometry and metamorphic *P–T* paths. In: *Evolution of Metamorphic Belts, Special Publication, 43* (eds Daly, J. S., Cliff, R. A. & Yardley, B. W. D.), pp. 63–82. Geological Society, London.

Spear, F. S., 1993. *Metamorphic Phase Equilibria and Pressure–Temperature–Time Paths*. Mineralogical Society of America Monograph, Washington, DC.

Spear, F. S. & Rumble, D., 1986. Pressure, temperature and structural evolution of the Orfordville Belt, west-central New Hampshire. *Journal of Petrology*, **27**, 1071–1093.

Spear, F. S. & Selverstone, J., 1983. Quantitative *P–T* paths from zoned minerals: theory and tectonic application. *Contributions to Mineralogy and Petrology*, **83**, 348–357.

Spear, F. S., Kohn, M. J. & Harrison, T. M., 1989. A thermal model for west-central New Hampshire. *Geological Society of America Abstracts with Program*, **21**, 67–68.

Spear, F. S., Hickmott, D. D. & Selverstone, J., 1990. Metamorphic consequences of thrust emplacement, Fall Mountain, New Hampshire. *Geological Society of America Bulletin*, **102**, 1344–1360.

Spear, F. S., Peacock, S. M., Kohn, M. J., Florence, F. & Menard, T., 1991. Computer programs for petrologic *P–T–t* path calculations. *American Mineralogist*, **76**, 2009–2012.

Spear, F. S., Kohn, M. J., Cheney, J. T. & Florence, F., 2002. Metamorphic, thermal, and tectonic evolution of central New England. *Journal of Petrology*, **43**, 2097–2120.

Strehlau, J. & Meissner, R., 1987. Estimation of crustal viscosities and shear stresses from an extrapolation of experimental steady state flow data. In: *Compositions, Structure and Dynamics of the Lithosphere–Asthenosphere System*, pp. 69–87. American Geophysical Union, Washington DC.

Symmes, G. H. & Ferry, J. M., 1992. The effect of whole-rock MnO content on the stability of garnet in pelitic schists during metamorphism. *Journal of Metamorphic Geology*, **10**, 221–237.

Taubert, P., 1988. *Abschatzung der genauigkeit von messergebnissen*. VEB Verlag Technik, Berlin.

Thompson, J. B., 1957. The graphical analysis of mineral assemblages in pelitic schists. *American Mineralogist*, **42**, 842–858.

Thompson, A. B. & England, P. C., 1984. Pressure–temperature paths of regional metamorphism, II: Their influence and interpretation using mineral assemblages in metamorphic rocks. *Journal of Petrology*, **25**, 929–954.

Turcotte, D. L. & Shubert, G., 1982. *Geodynamics. Applications of Continuum Physics to Geological Problems*. J Wiley & Sons, New York, NY.

Urbakh, V. Y., 1964. *Biometrical Methods*. Mir, Moscow (in Russian).

Vidal, O., Goffe, B., Bousquet, R. & Parra, T., 1999. Calibration and testing of an empirical chloritoid–chlorite Mg–Fe exchange thermometer and thermodynamic data for daphnite. *Journal of Metamorphic Geology*, **17**, 25–39.

Volobuev, M. I., Zykov, S. I. & Stupnikova, N. I., 1968. Yenisey folded region. In: *Precambrian Geochronology of Siberian Continental Plateau and its Folded Margin* (ed. Manujlova, M. M.), pp. 266–274. Nauka, Leningrad (in Russian).

Whitney, D. L., Lang, H. M., Ghent, E. D., 1995. Quantitative determination of metamorphic reaction history: mass balance between groundmass and mineral inclusion assemblages in metamorphic rocks. *Contributions to Mineralogy and Petrology*, **120**, 404–411.

Whitney, D. L., Mechum, T. A., Kuehner, S. M. & Dilek, Y. R., 1996. Progressive metamorphism of pelitic rocks from protolith to granulite facies, Dutchess County, New York, USA: constraints on the timing of fluid infiltration during regional metamorphism. *Journal of Metamorphic Geology*, **14**, 163–181.

Whitney, D. L., Miller, R. B. & Paterson, S. R., 1999. *P–T–t* evidence for mechanisms of vertical tectonic motion in a contractional orogen: north-western US and Canadian Cordillera. *Journal of Metamorphic Geology*, **17**, 75–90.

Wolfram, S., 2003. *The Mathematica Book*, 5th edn. Wolfram Media, Inc., Champaign, IL.

Zlobin, V. A., Kulikov, A. A. & Bobrov, V. A., 1975. Objective laws of distribution of radioactive elements in Precambrian suits of Yenisey Range. In: *Radioactive Elements in Rocks* (ed. Kuznetsov, V. A.), pp. 198–203. Nauka, Novosibirsk (in Russian).

Zvyagina, E. A., 1989. *Metamorphism and gold-bearing deposit of Verkhne–Enaschimsk ore node*. PhD Thesis, Irkutsk University Press, Russia (in Russian).